AFRL-RB-WP-TP-2012-0197

HIFiRE-1 PRELIMINARY AEROTHERMODYNAMIC MEASUREMENTS (POSTPRINT)

Roger L. Kimmel and David W. Adamczak

High-speed Aerodynamic Configuration Branch
Aeronautical Sciences Division

MAY 2012

STINFO COPY

AIR FORCE RESEARCH LABORATORY
AIR VEHICLES DIRECTORATE
WRIGHT-PATTERSON AIR FORCE BASE, OH 45433-7542
AIR FORCE MATERIEL COMMAND
UNITED STATES AIR FORCE

REPORT DOCUMENTATION PAGE

1. REPORT DATE (DD-MM-YY)	2. REPORT TYPE	3. DATES COVERED (From - To)
May 2012	Conference Paper Postprint	01 May 2010 – 01 May 2012

4. TITLE AND SUBTITLE
HIFiRE-1 PRELIMINARY AEROTHERMODYNAMIC MEASUREMENTS (POSTPRINT)

5a. CONTRACT NUMBER
In-house

5b. GRANT NUMBER

5c. PROGRAM ELEMENT NUMBER
61102F

6. AUTHOR(S)
Roger L. Kimmel and David W. Adamczak

5d. PROJECT NUMBER
2307

5e. TASK NUMBER

5f. WORK UNIT NUMBER
A0HY0A

7. PERFORMING ORGANIZATION NAME(S) AND ADDRESS(ES)
High-speed Aerodynamic Configuration Branch
Aeronautical Sciences Division
Air Force Research Laboratory, Air Vehicles Directorate
Wright-Patterson Air Force Base, OH 45433-7425
Air Force Materiel Command, United States Air Force

8. PERFORMING ORGANIZATION REPORT NUMBER
AFRL-RB-WP-TP-2012-0197

9. SPONSORING/MONITORING AGENCY NAME(S) AND ADDRESS(ES)
Air Force Research Laboratory
Air Vehicles Directorate
Wright-Patterson Air Force Base, OH 45433-7425
Air Force Materiel Command
United States Air Force

10. SPONSORING/MONITORING AGENCY ACRONYM(S)
AFRL/RBAH

11. SPONSORING/MONITORING AGENCY REPORT NUMBER(S)
AFRL-RB-WP-TP-2012-0197

12. DISTRIBUTION/AVAILABILITY STATEMENT
Approved for public release; distribution unlimited.

13. SUPPLEMENTARY NOTES
Conference paper published in the Proceedings of the 41st AIAA Fluid Dynamics Conference and Exhibit held in Honolulu, Hawaii, June 26, 2011.
PA Case Number: 88ABW-2011-3317; Clearance Date: 13 Jun 2011. Paper contains color.

14. ABSTRACT
The Hypersonic International Flight Research Experimentation (HIFiRE) program is a hypersonic flight test program executed by the Air Force Research Laboratory (AFRL) and Australian Defence Science and Technology Organisation (DSTO). HIFiRE flight one flew in March 2010. Principle goals of this flight were to measure hypersonic boundary-layer transition and shock boundary layer interactions in flight. The flight successfully gathered pressure, temperature and heat transfer measurements during ascent and reentry. HIFiRE-1 has provided transition measurements suitable for calibrating N-factor prediction methods for flight, and has produced some insight into the structure of the transition front on a cone at angle of attack. Pressure and heat transfer measurements in the shock-boundary-layer interaction were obtained. Preliminary analysis of the shock boundary layer interaction shows intermittent pressure fluctuations qualitatively similar to those measured in wind tunnel experiments. A large amount of data was obtained on the flight, and significant data reduction efforts continue.

15. SUBJECT TERMS
boundary layer transition, hypersonic, flight test

16. SECURITY CLASSIFICATION OF:			17. LIMITATION OF ABSTRACT:	18. NUMBER OF PAGES	19a. NAME OF RESPONSIBLE PERSON (Monitor)
a. REPORT Unclassified	**b. ABSTRACT** Unclassified	**c. THIS PAGE** Unclassified	SAR	42	Roger L. Kimmel **19b. TELEPHONE NUMBER** (Include Area Code) N/A

HIFiRE-1 Preliminary Aerothermodynamic Measurements

Roger L. Kimmel[*] David Adamczak[†]
Air Force Research Laboratory, 2130 8th St., WPAFB, OH 45433, USA

The Hypersonic International Flight Research Experimentation (HIFiRE) program is a hypersonic flight test program executed by the Air Force Research Laboratory (AFRL) and Australian Defence Science and Technology Organisation (DSTO). HIFiRE flight one flew in March 2010. Principle goals of this flight were to measure hypersonic boundary-layer transition and shock boundary layer interactions in flight. The flight successfully gathered pressure, temperature and heat transfer measurements during ascent and reentry. HIFiRE-1 has provided transition measurements suitable for calibrating *N*-factor prediction methods for flight, and has produced some insight into the structure of the transition front on a cone at angle of attack. Pressure and heat transfer measurements in the shock-boundary-layer interaction were obtained. Preliminary analysis of the shock boundary layer interaction shows intermittent pressure fluctuations qualitatively similar to those measured in wind tunnel experiments. A large amount of data was obtained on the flight, and significant data reduction efforts continue.

Nomenclature

Symbols

A = disturbance amplitude, dimensionless
A_0 = disturbance amplitude at lower neutral bound, dimensionless
C_h = heat transfer coefficient (Stanton number), $\dot{q}/\rho_\infty U_\infty (H_0 - H_w)$, dimensionless
C_p = specific heat, J/kg K
f = frequency, Hz
h = altitude, m
H = specific enthalpy, J/kg
k = thermal conductivity, W/mK
L = reference length from stagnation point to flare / cylinder corner, 1.6013 m full scale
M = freestream (upstream of vehicle shock) Mach number
N = $\ln[A(f)/A_1(f)]$, dimensionless
p = pressure, kPa
p' = fluctuating pressure (instantaneous departure from local mean), kPa
δp = pressure zero-shift at t=60 seconds, kPa
$\dot{q}$ = heat transfer rate, W/m^2
Re = freestream unit Reynolds number per meter, $\rho_\infty U_\infty / \mu_\infty$
s = streamwise surface arc length from stagnation point, m
t = time after liftoff, seconds
T = temperature, K
U = magnitude of the velocity vector, m/s
v = velocity component normal to missile x-axis, m/s
x = distance from stagnation point along vehicle centerline, m
y = vertical (pitch-plane) coordinate, or depth below model wetted surface m
α = thermal diffusivity, $k/\rho C_p$, m^2/s
Φ = wind-fixed angular coordinate around vehicle circumference, Φ=0 on windward stagnation line, degrees (Figure 11)

---

[*] Principal Aerospace Engineer, Associate Fellow AIAA.
[†] Senior Engineer, Member AIAA

Approved for public release; distribution unlimited

ϕ = body-fixed angular coordinate around vehicle circumference, $\phi = 0$ on primary instrumentation ray, degrees (Figure 11)

ρ = density, kg/m^3

μ = viscosity, N s / m^2

Subscripts

0 = stagnation conditions

1 = lower neutral bound

m = measured in flight

e = evaluated at boundary-layer edge

tr = transition location

w = evaluated at model wall

x = evaluated at distance x from stagnation point

∞ = freestream conditions, upstream of model bow shock

Acronyms

AFRL	Air Force Research Laboratory
AoA	angle of attack
AOSG	Aerospace Operational Support Group, Royal Australian Air Force
ARC	Ames Research Center
AVD	Air Vehicles Division
BC	boundary condition
BEA	best estimated atmosphere
BET	best estimated trajectory
BLT	boundary-layer transition
CUBRC	Calspan University of Buffalo Research Center
DFRC	Dryden Flight Research Center
DSTO	Defence Science and Technology Organisation
GPS	Global Positioning System
HIFiRE	Hypersonic International Flight Research and Experimentation
HT	heat transfer
LaRC	Langley Research Center
NIST	National Institute of Standards and Technology
OMC	optical mass catpure
PHBW	pressure, high bandwidth
PLBW	pressure, low bandwidth
PSD	power spectral
RANRAU	Royal Australia Navy Ranges and Assessing Unit
SBLI	shock boundary-layer interaction
TLBW	temperature, low bandwidth
TM	telemetry
TZM	titanium-zirconium-molybdenum
UTC	Universal Coordinated Time
WSMR	White Sands Missile Range

I. Introduction

The Hypersonic International Flight Research Experimentation (HIFiRE) program is a hypersonic flight test program executed by the United States AFRL and the Australian DSTO.[1,2] Its purpose is to develop and validate technologies critical to next generation hypersonic aerospace systems. Candidate technology areas include, but are not limited to, propulsion, propulsion-airframe integration, aerodynamics and aerothermodynamics, high temperature materials and structures, thermal management strategies, guidance, navigation, and control, sensors, and system components. The HIFiRE program consists of extensive ground tests and computation focused on specific hypersonic flight technologies. Each technology program is designed to culminate in a flight test. The first science

flight of the HIFiRE series, HIFiRE-1, launched 22 March 2010 at the Woomera Prohibited Area in South Australia at 0045 UTC (1045 local time).

The primary objective of HIFiRE-1 was to measure aerothermal phenomena in hypersonic flight. The primary experiment consisted of boundary-layer transition measurements on a 7-deg half angle cone with a nose bluntness of 2.5 mm radius. The secondary aerothermal experiment was a shock-boundary-layer interaction created by a 33-deg-flare / cylinder configuration. HIFiRE-1 ground test and computation created an extensive knowledge base regarding transition and SBLI on axisymmetric bodies. This research has been summarized in numerous prior publications.[3,4,5,6,7,8,9,10,11,12,13,14] A companion paper presents initial *N*-factor calculations for the HIFiRE-1 BLT flight experiment.[15]

This paper reports preliminary BLT and SBLI results. Since BLT was the primary experiment, it is the focus of this paper. Some initial SBLI results are presented as examples of the data obtained during flight. HIFiRE-1 yielded over 1.6 gigabytes of data. Its analysis in some cases is complex due to complications that arose during flight. Therefore, additional analysis remains to be performed for both the BLT and SBLI experiments. Several interesting and unexpected phenomena were observed during flight, and they merit further scrutiny. The HIFiRE-1 data will be available to researchers for further investigation.

II. Vehicle and Trajectory

The HIFiRE-1 vehicle has been described in several prior publications, most notably in Ref. 14. The overall payload dimensions and the different payload modules are shown in Figure 1. The experiments were carried out on the forward sections of payload including a cone, a cylinder, and a flare which transitions to the diameter of the second stage motor (0.356 m). The cone half angle of seven degrees was chosen to match configurations used in preceding ground tests and analytical/numerical work. One side of the cone incorporated a diamond-shaped trip element to create roughness-induced transition. The flare angle of 33° was chosen to induce turbulent boundary-layer separation and reattachment on the flare face4 as was observed during wind tunnel testing. Two cutout channels in the flare, one of which is visible in the bottom of Figure 1, contained a laser-diode absorption spectrometry experiment that was discussed in a prior publication.[16]
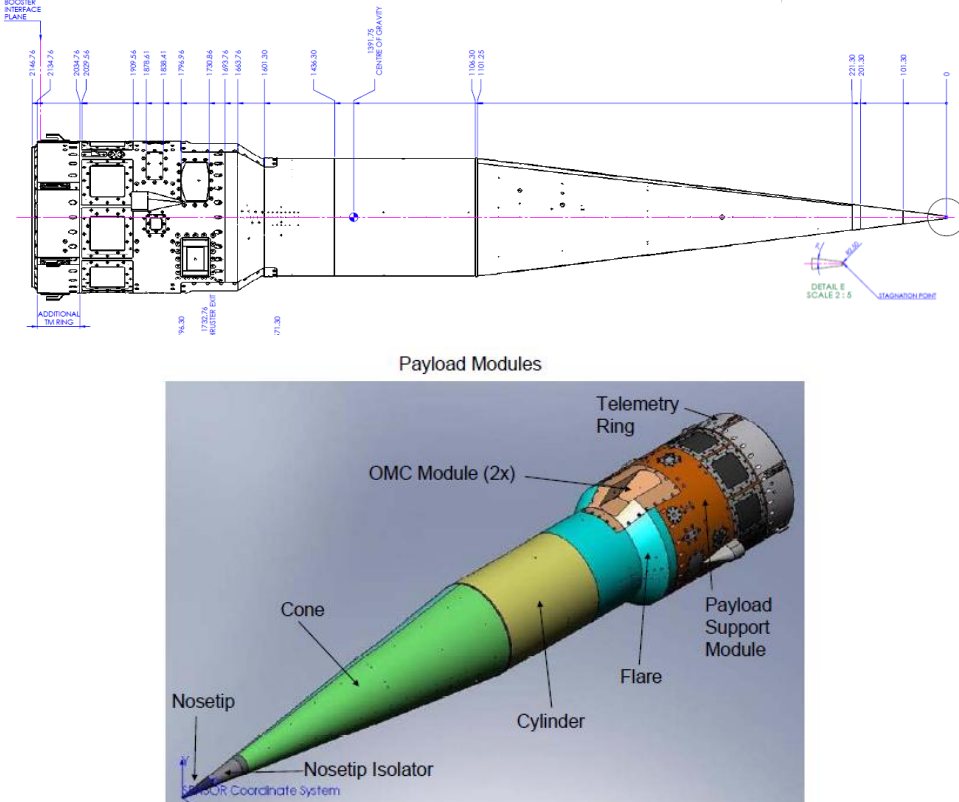

Figure 1 HIFiRE-1 payload configuration, dimensions in mm

The launch vehicle for the HIFiRE-1 payload was a Terrier Mk70 booster–Improved Orion sustainer[17] motor combination. The Terrier and Orion motors have been sourced from surplus military ordnance used extensively in sounding rocket programs. This motor combination was chosen to minimize overall program costs and, based on past flight experience, to deliver a Mach number between seven and eight during the experiments. Booster and sustainer were passively spin-stabilized using fin cant on the individual stages to minimize trajectory dispersion. Total payload weight was 135 kg with an all-up flight segment weight of 1554 kg and a total stack length of just over 9 meters (Figure 2).
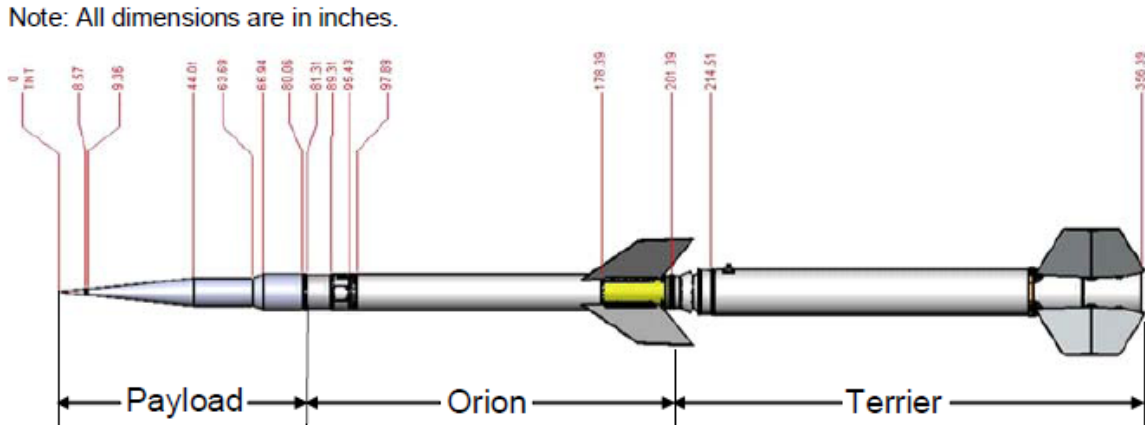
Note: All dimensions are in inches.

Figure 2 HIFiRE Flight one booster stack

The payload flew a ballistic trajectory similar to those employed for the HyShot[18] and HyCAUSE[19] flights. The as-flown trajectory is shown in Figure 3. The Terrier first stage burnt for 6.3 seconds and was then drag-separated from the second stage. The Orion/payload stack coasted until the second stage ignited at 15 seconds. Orion burnout occurred at 43 seconds. The payload remained attached to the second stage throughout the entire flight to provide stability as the payload reentered the atmosphere. Approximately the first and last 45 seconds of the trajectory were endoatmospheric. The remainder of the trajectory was exoatmospheric. During the exoatmospheric phase of the trajectory the Orion/payload stack was to have been reoriented with the reentry flight path angle. This was to have been accomplished using two nitrogen cold gas thrusters and a process employed for the reorientation of spinning satellites as presented by Wiesel.[20]

A prior publication describes the HIFiRE-1 mission.[21] The most notable complications in the mission with regard to its science objectives were failures of the on-board GPS and the exoatmospheric pointing maneuver, and drift in the cone thermocouples. The loss of the GPS meant that the vehicle altitude and velocity had to be reconstructed from existing data such as accelerometers, radar tracks, etc. Reference 21 describes development of the BET. The failure of the exoatmospheric pointing maneuver was a more serious malfunction, since it caused the vehicle to enter the atmosphere with an angle of attack as high as 40-deg. Although angle-of-attack oscillations damped and decreased as the vehicle encountered higher density air at lower altitudes, the payload was still at over 10-deg AoA as aerothermal data began to be collected during descent. Since the risk of this occurrence was recognized prior to flight, the payload flew unshrouded, i.e. no nosecone shell covered the experiment during ascent. This permitted low-angle-of-attack (< 1 deg) data to be obtained during ascent. Although the descent phase was intended as the design point for HIFiRE-1 data acquisition, at least a portion of the ascent appears to have yielded useful, low angle-of-attack data. The Orion/payload stack remained in stable flight until impact.

Following ascent, most of the thermocouples in the cone began to drift upward. Many drifted until these channels saturated. The cause of this drift was presumed to be due to temperature effects on the thermocouple amplifier chips. Thermocouples in the SBLI experiment did not exhibit this shift. The drift in the BLT thermocouples means that absolute temperature data on the cone during descent cannot be measured. Thermocouples that saturated provided no data. However, qualitative trends during descent, including transition, may be extracted from thermocouples that did not saturate.
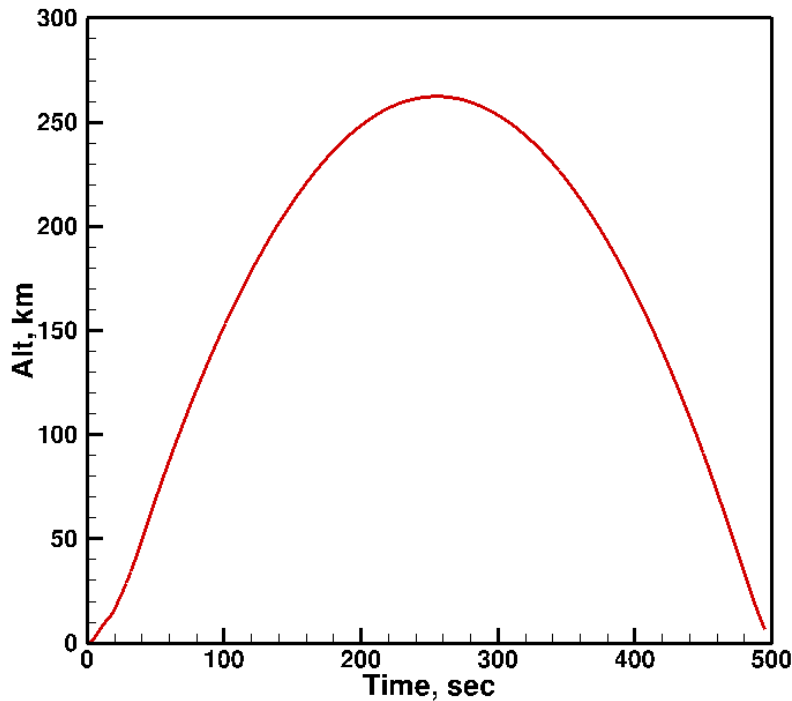
Figure 3 HIFiRE-1 as-flown trajectory

III.   Instrumentation

The primary aerothermal instrumentation for HIFiRE-1 consisted of Medtherm Corporation coaxial thermocouples. Type T (copper-constantan) thermocouples were installed in aluminum portions of the aeroshell and Type E (chromel-constantan) were installed in the steel portions. Kulite® pressure transducers measured local static pressures. Several pressure transducers were operated in differential mode to measure differential pressures 180-deg apart on the vehicle to aid in attitude determination. Other transducers were referenced to internal pressure and sampled at up to 60 kHz to measure high-frequency pressure fluctuations. Figure 4 - Figure 7 illustrate the transducer layout. In these figures, TLBW refers to Medtherm coaxial thermocouples, PLBW refers to Kulite® pressure transducers sampled at 400 Hz, and PHBW refers to Kulite® pressure transducers sampled at up to 60 kHz. Heat transfer transducers HT1, HT2, HT6 and HT7 were Medtherm Schmidt-Boelter gauges sampled at 400 Hz. HT3 and HT8 were Vatell Corporation thin-film thermopile heat transfer gauges sampled at 4 kHz. HT5 and HT10 were ITA Inc. Delta-T gauges sampled at 400 Hz.

All pressure transducers with the exception of the flare were model XCE-093. Those in the flare were XTEH-7LAC-190 (M). The flare transducers each output separate AC and DC-coupled signals that were digitized on different channels.

The coaxial thermocouples were dual-junction models that measured front-surface and back-surface (internal) temperatures simultaneously. These thermocouples were bonded into pre-drilled holes in the model surface using LOCTITE® adhesive. The thermocouples were installed with the backface junction flush to within 0.1 mm (estimated) of the model interior surface. The portion of the thermocouple which extended beyond the model external surface was removed using files and abrasives so that the final thermocouple contour matched the model surface contour. This finishing process created a "sliver junction" between the center-wire and annular thermocouple materials, in which whiskers of one conductor are dragged over the other to create the thermocouple junction.
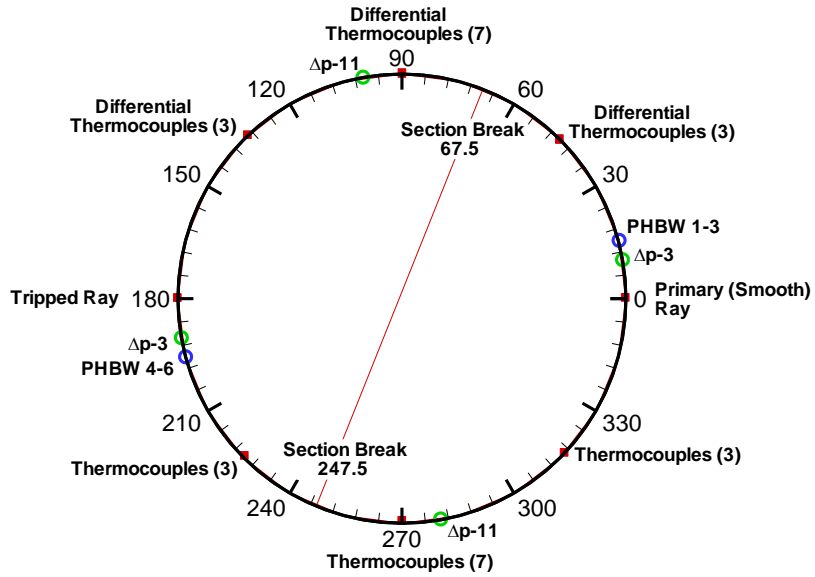
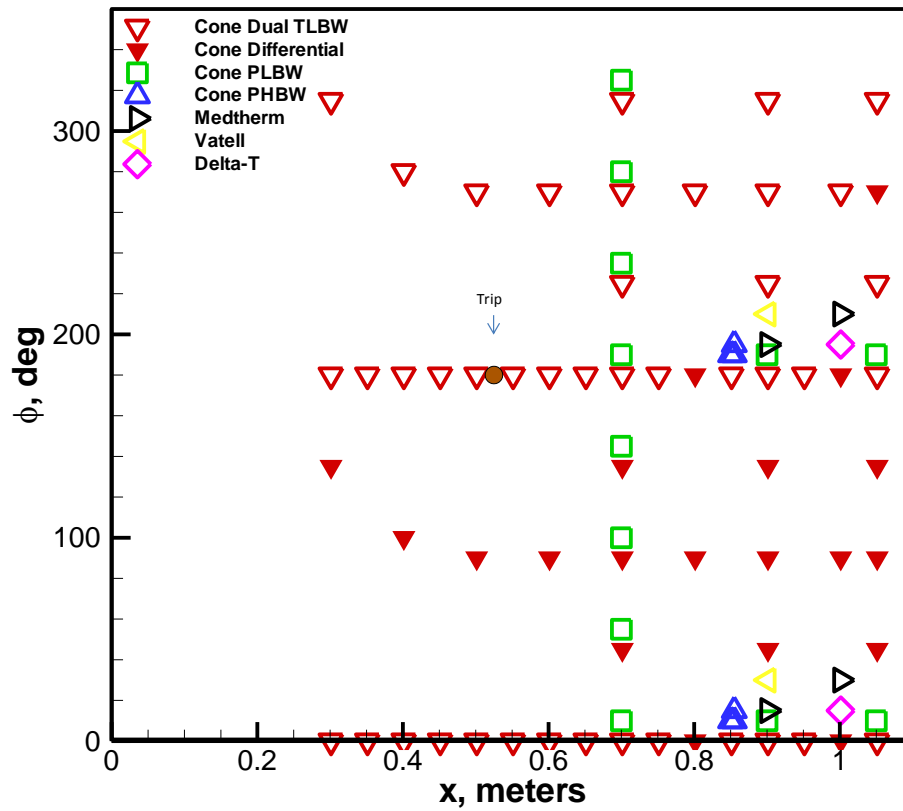**Figure 4 HIFiRE-1 radial transducer layout**

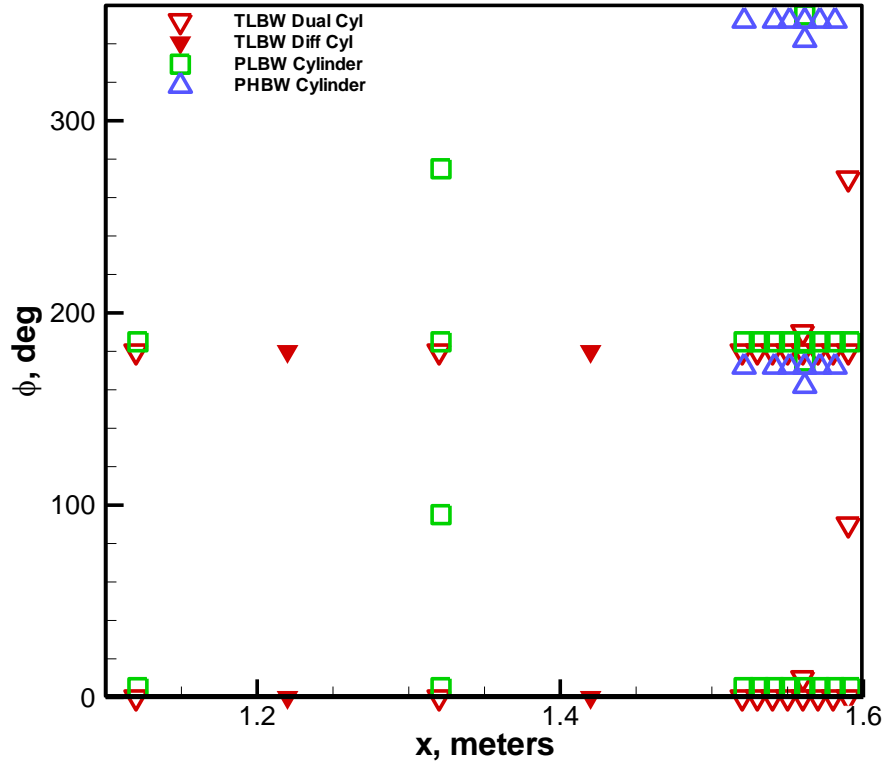**Figure 5 HIFiRE-1 Cone transducer layout detail.**

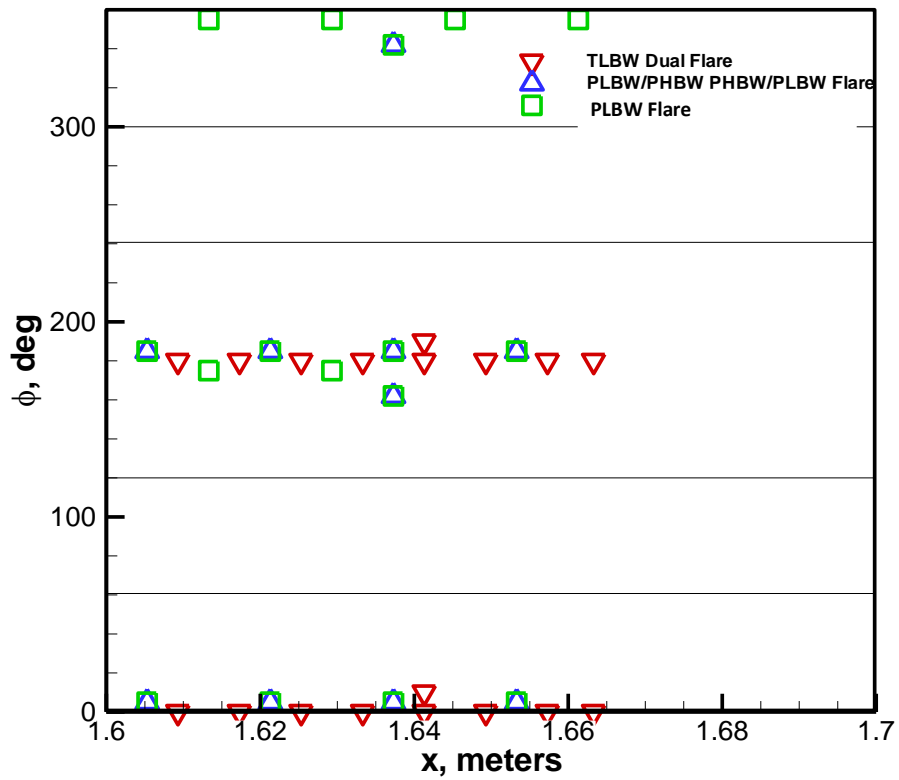**Figure 6 HIFiRE-1 cylinder transducer layout detail**

Figure 7 HIFiRE-1 flare transducer layout detail

IV. Data Analysis

Data analysis for the HIFiRE-1 flight required development of a best-estimated atmosphere (BEA), best-estimated trajectory (BET) and vehicle attitude estimate. A prior paper describes the BEA and BET development.[21] Table 1 presents maximum estimated percentage errors in the BEA quantities at the data point nearest 27 km altitude. Uncertainty increases with increasing altitude. Since all data was taken below 27 km, the Table 1 uncertainties are worst-case. Also, uncertainty was much higher for the descent phase of the flight. No uncertainty estimate is currently available for the BET parameters. Comparison of the AFRL BET with a BET independently developed by NASA DFRC however, gives some measure of uncertainty levels. Table 2 summarizes deviations between the two BETs at critical times during ascent and descent.

Table 1 BEA uncertainties at 27 km

	p	ρ	T	Wind Speed
Ascent	4.10%	1.40%	0.40%	2.8 m/s
Descent	26.80%	25%	2.70%	16.5 m/s

Table 2 Deviations between AFRL and NASA BETs

Time, sec	Δh, m	ΔM	ΔRe, %
21.5	212	0.073	2.6
483.5	244	0.16	6.3

HIFiRE-1 transmitted data on three telemetry streams. With the exception of TM stream one, which consisted mostly of rough-side transducers, transmission quality was good. TM stream one was very noisy, with dropouts and bit shifts, which degraded the quality of data on this channel. Also on this channel, the flight computer dedicated to thermocouples on the cylinder upstream of the flare on the tripped side of the payload failed during ascent, so those data were lost.

Analysis of the thermocouple and pressure data consisted of first removing demonstrably bad points due to TM dropouts. Thermocouple data, which was originally processed using a linear calibration, was re-calibrated to account for nonlinearities in the thermocouple calibrations using standard NIST calibration coefficients for type T and type E thermocouples. The maximum nonlinear correction for the T thermocouples during ascent was about 5 deg K. The maximum nonlinear correction for the Type E thermocouples was about 33 deg K, for thermocouples near attachment in the SBLI. The amount of correction depended on temperature and type of thermocouple. SBLI thermocouples required greater adjustment due to their higher temperature.

Heat transfer analysis required that the thermocouple data be smoothed. Where data points were missing, data was linearly interpolated between good points, so that input data for the heat transfer analysis were evenly spaced in time. Back face temperatures were zero-shifted so that the average temperatures of the front and back face thermocouples for the first 0.1 seconds of data were coincident. The data were smoothed using a simple moving average of 0.2 seconds.

Heat transfer was estimated using inverse analysis. Radiation was not considered since it was estimated to be less than 1% of convective heat transfer during periods of interest in the flight. Heat transfer at the aeroshell front face (wetted surface) was derived from the one-dimensional conduction equation

$$\dot{q} = k \frac{\partial T}{\partial y}$$

The temperature distribution through the aeroshell was obtained by solving the transient conduction equation

$$\frac{\partial T}{\partial t} = \alpha \frac{\partial^2 T}{\partial y^2}$$

The transient conduction equation requires front and back face boundary conditions. The time-history of the front face was used as one BC. Both adiabatic conditions and measured back face temperature histories were tested as back face BCs. Both gave essentially the same results, although esults using adiabatic backface conditions were slightly more consistent. The adiabatic backface condition was thus used for most analysis in this paper. All

analysis was carried out using material properties for the shell material, 6061 T6 aluminum for the cone and upstream portion of the cylinder, and AISI 1045 steel for the downstream portion of the cylinder and the flare.

The use of the adiabatic back face BC was also tested by using measured front face temperatures as inputs to a 1D thermal conduction model of the aeroshell in the TOPAZ finite element conduction solver. The measured front face temperatures were used as a temperature BC, and the back face was treated as adiabatic. Figure 8 presents the results of two such computations at x=0.3 m and x=1.05 m. The computed back face temperature generally agreed well with the measured temperature up to about 10-15 seconds. After this time the measured back face temperature is somewhat lower than would be expected from an adiabatic back face condition. Although the difference between the expected adiabatic backface temperature and the measured temperature is less than 5 degrees, this is enough to create large percentage errors at low heating levels. Measured turbulent heat transfer rates are within about 25% of heating predicted using the van Driest[22] theory and BET conditions. A similar comparison shows laminar heating with +/-70% of predictions using the Eckert[23] method. Multiple sources may account for these discrepancies, such as transducer drift, mislocation of the back face thermocouple, multi-dimensional conduction effects, non-planar geometry effects, or backface conduction. The effect of the detailed transducer geometry was assessed by gridding a detailed model of the coaxial thermocouple gauge as it was embedded in the aluminum wall, including the LOCTITE® bonding material, and performing the same calculation described above. The effect of the transducer details was negligible.
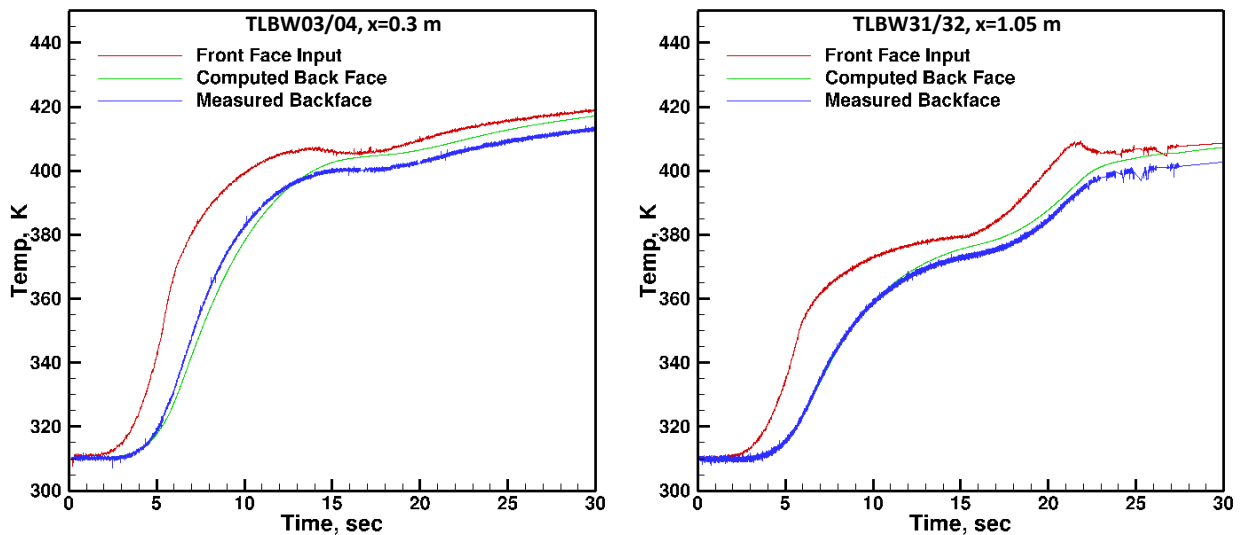

Figure 8 Examination of adiabatic backface boundary condition.

Pressure measurements recorded after the vehicle left the atmosphere revealed some zero-shift. This zero-shift was determined by averaging the pressure for a given sensor over a 0.2 second window centered at t = 60 sec (h = 88600 km). This zero shift was assumed to be linear with time during the launch, and the appropriate increment at a given time was then subtracted from the measured signal:

$$p = p_m - \frac{t}{60} \delta p$$

Figure 9 compares the surface pressure measured on four transducers to the Taylor-Maccoll solution[24] for surface pressure on a 7-deg sharp cone. The measured pressures are generally within 6% of the Taylor-Maccoll solution. This agreement provides a-posteriori validation of the BET. The periodic fluctuations in pressure, most notable for t> 20 seconds, are due to vehicle spin combined with small angle of attack. The scatter in pressure for t<6 seconds is attributed to acceleration sensitivity of the transducers.

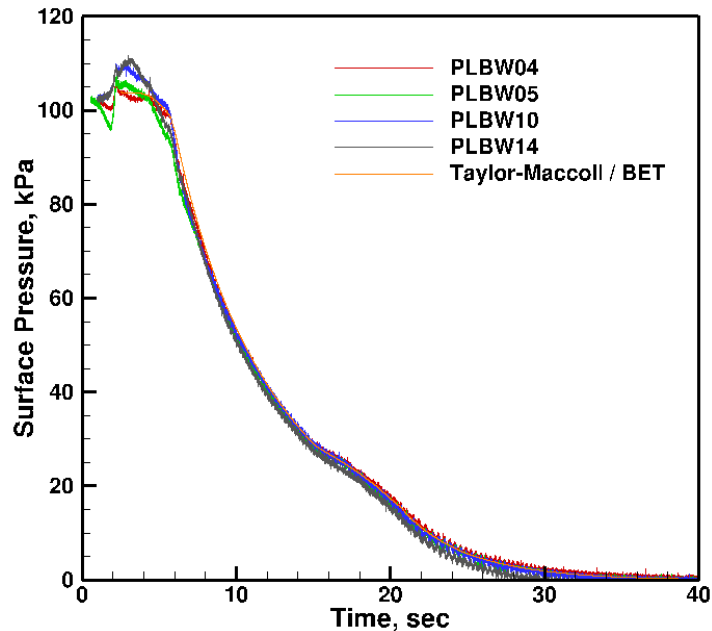Approved for public release; distribution unlimited

Figure 9 Cone surface pressure during ascent

A similar procedure was applied to surface pressures recorded during reentry. Since in this case there was no ground-level reference, the correction consisted of a scalar shift so that transducers read zero at 456 seconds (h=80 km). The results of this data treatment are compared to Taylor-Maccoll solutions based on the AFRL and NASA BETs in Figure 10. Large oscillations in pressure due to the high AoA reentry are apparent. The extrema of the measured pressures bracket solutions from both BETs, but the NASA BET appears to better approximate the mean. The NASA BET was thus used for all analysis described in this paper. PLBW04 appears to drift for t> 485 seconds.

The vehicle orientation in flight is described by the velocity-referenced coordinate system shown in Figure 11. Roll angle, Φ, is defined as the angle between the ϕ=0 primary instrumentation ray and the velocity component normal to the missile long axis, positive counter-clockwise as viewed from the front of the payload. The vehicle spin in flight was counter-clockwise, as determined from inspection of surface pressures, ground cameras and other on-board sensors. Angle of attack and roll angle were determined from measured cone surface pressures. The vehicle rotated on its long axis, which in turn executed a coning motion or precession about the flight path.[25] The coning period is much longer than the spin period, so the orientation of any given transducer may be approximated as a rotation from windward to leeward and back again at constant AoA. This motion created a surface pressure that was usually a sinusoidal function in time, although at some times other lower-amplitude harmonics are evident in the pressure signal, indicating a somewhat more complicated motion. The fluctuating component of the surface pressure measured with absolute pressure transducers was determined by taking a moving average of the pressure and then subtracting this from the instantaneous pressure. Differential pressure transducers also measured the pressure difference between two ports 180 apart on the cone. Two differential transducers monitored four ports, but one transducer malfunctioned, leaving only one differential pressure measurement.

Several schemes were examined to determine the roll angle. Although all gave similar answers, the simplest and most satisfactory method was to locate the local maxima and minima in the differential pressure, and assume a constant roll rate (linear phase variation in time) between these two points. The spin rate varied from about 6 Hz just after first stage burnout at 8.5 seconds, to 3.7 Hz at 30 seconds. During reentry, spin rate varied from about 4 Hz at 470 seconds to 3.5 Hz at 485 seconds. These roll rates, which are referenced to velocity, are slightly different from those extracted from the horizon sensors or magnetometers, which are earth-referenced.[21]
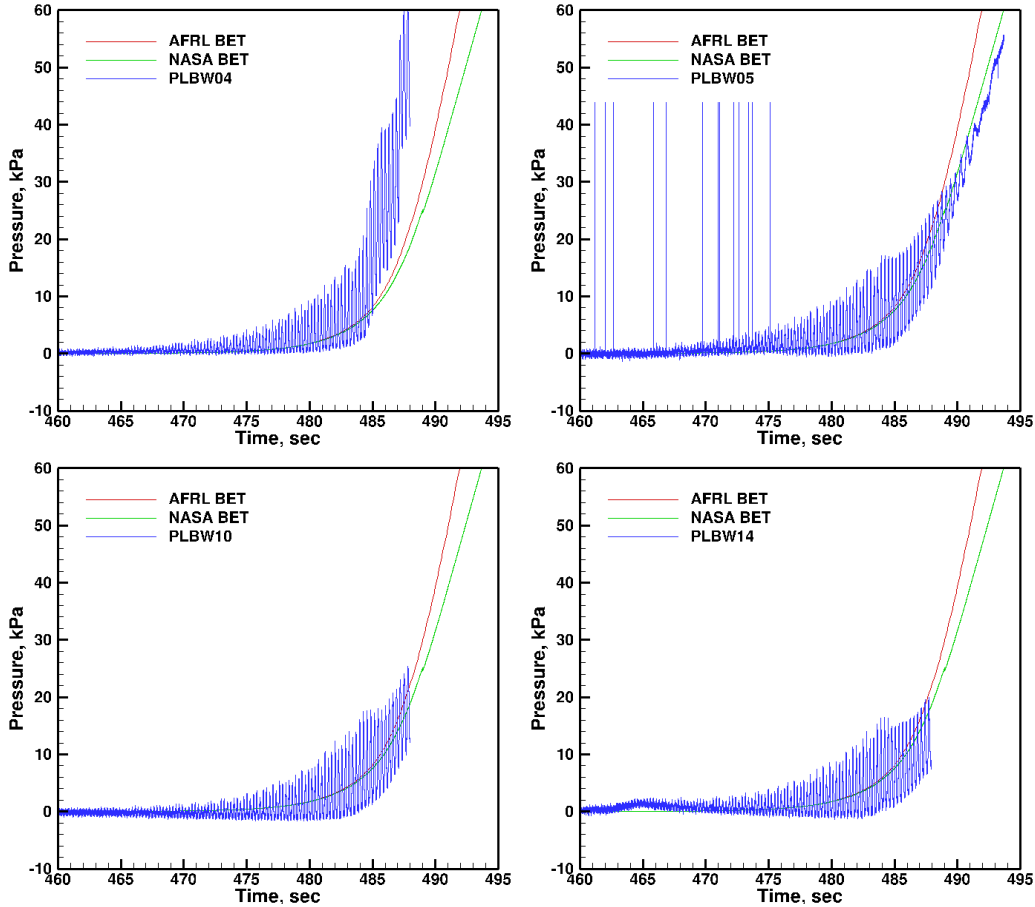
Figure 10 Measured cone surface descent-phase pressures compared to Taylor-Maccoll solutions derived from AFRL and NASA BETs.
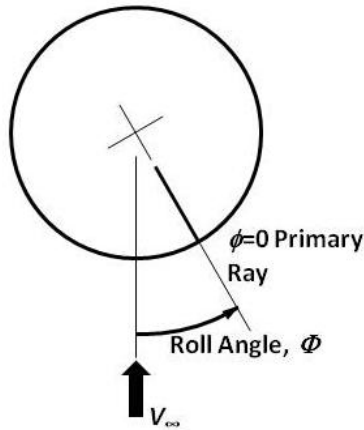
Figure 11 Roll angle definition

Angle of attack was similarly estimated by taking local extrema in pressure for each transducer, and then interpolating AoA from tabulated values of cone pressure and Mach number. The estimated AoA was then obtained by averaging over the transducers. Figure 12 illustrates these results. During ascent, AoA was less than 0.5 deg for $t<21$ seconds, and less than 1-deg for $t<22$ seconds. During descent, AoA varied from 5-13 deg for $482< t<485$ seconds. The estimated uncertainty for AoA is 0.3-deg for ascent ($t<22$ sec) and 2.7 deg for descent ($t>483$ sec). This uncertainty is derived from the RMS variation in calculated AoA among the transducers. Some of the relatively large variation in AoA during reentry is due to the assumption of a simple harmonic motion of the missile.

In addition to executing a spinning and coning motion, the vehicle was also nutating and oscillating in pitch. Some of this complex motion is reflected in a modulation of the pressure fluctuations observed in Figure 10.
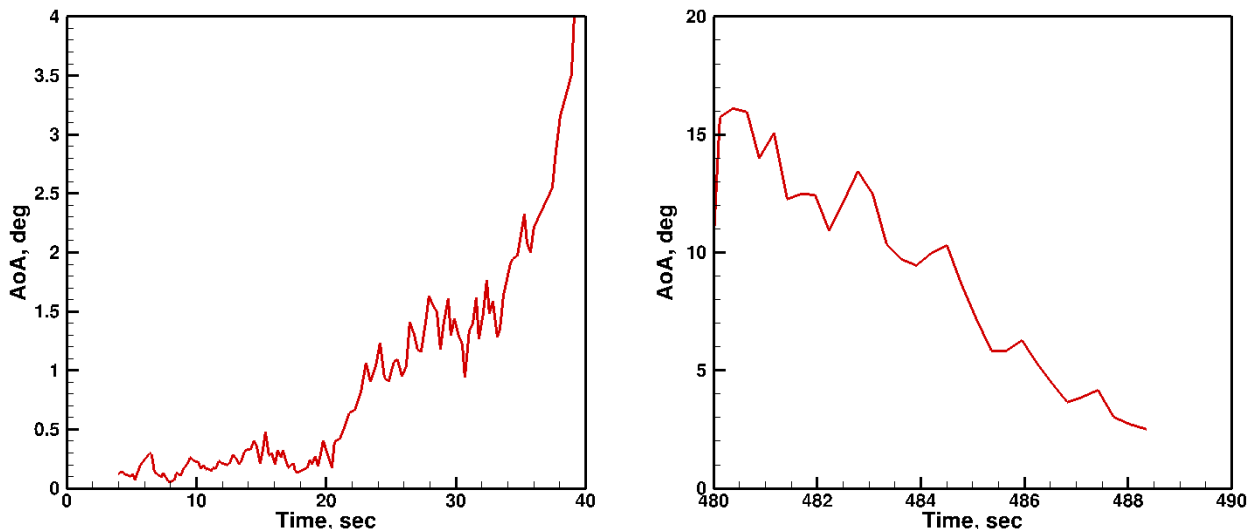

Figure 12 Angle of attack

V.   Transition Results

The Mach number and Reynolds number varied non-monotonically through the ascent due the motor burns. Figure 13 shows that Mach and Reynolds initially increased as the first stage burnt. Freestream Mach number and Reynolds number are derived from the BET and BEA, and the boundary-layer edge values are determined from a Taylor-Maccoll solution for a sharp cone of seven degree half-angle. The edge unit Reynolds number peaked at over 65×10^6 per meter at first-stage burnout at $t=6$ seconds. Mach and Reynolds then dropped as the vehicle coasted until $t=15$ seconds, when the second stage fired. At this point Mach and Reynolds both began to climb, until about $M=4.7$. After this the Reynolds number dropped rapidly as the vehicle escaped the atmosphere.
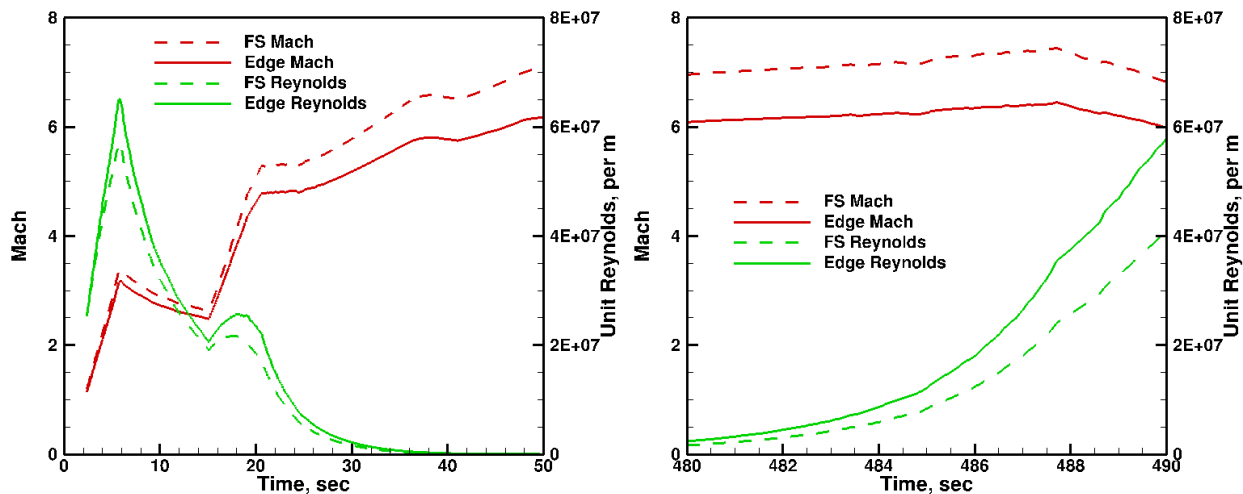
Figure 13 Ascent (left) and descent (right) Mach and Reynolds number flight histories

The wall condition throughout the flight was a cooled wall. Figure 14 illustrates the T_w/T_e and T_w/T_0 history throughout ascent for TLBW31 at $x=1.0513$ m. These ratios at other x-stations on the cone were similar to those presented in Figure 14, since there was little temperature variation over the length of the cone frustum. The ratio T_w/T_0 decreased throughout first-stage burn, then increased during the coast phase. T_w/T_0 decreased sharply during the initial second stage burn, then continued to decrease at a slower rate during the sustain portion of the second stage burn. This ratio was approximately 25% by $t=30$ seconds.

Figure 14 Ascent wall temperature compared to edge and stagnation temperatures at *x*=1.0513 m.

During ascent, the cone boundary-layer was turbulent over most of the vehicle shortly after it left the rail. This transition front then progressed downstream over the cone as the vehicle ascended and Reynolds number dropped. During reentry, this movement of the transition front was in the reverse direction, from rear to front of the vehicle. The ascent transition front mo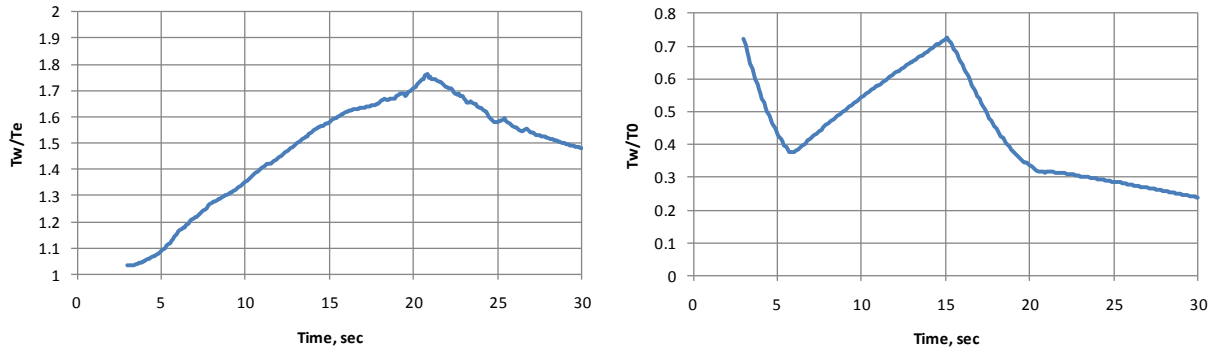vement is somewhat at odds conceptually from what we are familiar with in flight tests and wind tunnel experiments, and this creates some difficulty with nomenclature. For simplicity, the point at which the boundary-layer appeared to be fully laminar will be referred to as "transition onset." The last fully turbulent point will be referred to as "transition end" even though transition "end" preceded "onset" during the ascent.

The turbulent flow early in flight probably arose from a trip near the nose. Figure 15 shows heat transfer as a function of time, derived from temperature measurements on the smooth side of the cone. Expected turbulent and laminar heat transfer derived from Eckert and van Driest theories at *x*=0.3 m are shown for reference. The expected heat transfer was computed using the measured cone temperatures and BET conditions. The trends in expected heat transfer follow the Mach / Reynolds characteristics described above. The data show that heat transfer at these two transducers (*x*=0.3013 and 0.5013 m) transitioned from laminar to turbulent values nearly simultaneously at about *t*=13.5 seconds. This rapid movement of the transition front is consistent with tripped flow. The two transducers at *x*=0.5513 and 0.6013 m were damaged before flight and did not produce data. Flow over the transducer at *x*=0.6513 m remained turbulent beyond 13.5 seconds until about 15 seconds, when it appears to have transitioned to laminar.
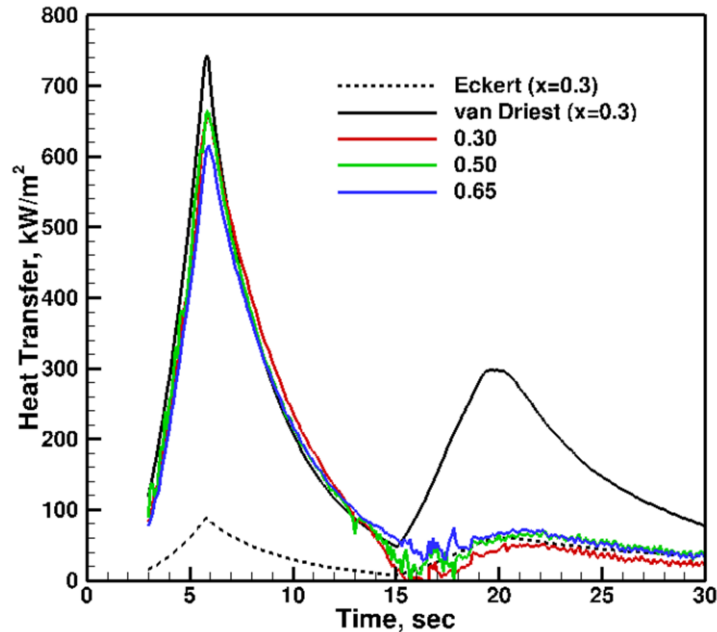

Figure 15 Ascent heat transfer for three smooth side (ϕ=0) thermocouples

The suspected source of the trip during the early portions of flight was one or more backward-facing steps in the nose assembly. The nose assembly, shown in Figure 16, consisted of the TZM nosetip and steel isolator, and was attached to the aluminum cone frustum by a stainless-steel joiner. To prevent steps from occurring at these joints during flight due to differential thermal expansion, small backward-facing steps were designed into the joints at room temperature. The steps were sized so that the joints would be flush with no steps at 23 km during reentry.
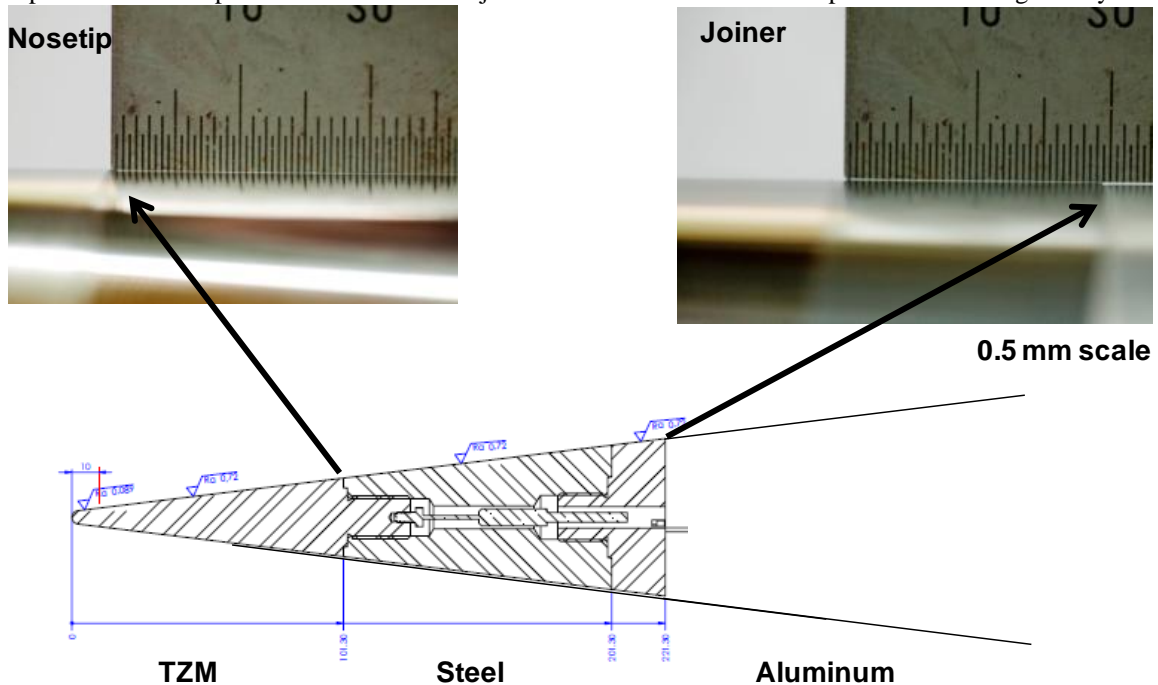
Figure 16 Nose assembly showing backward-facing steps for thermal expansion. Scale in photos is 0.5 mm

The as-manufactured steps were measured in the DSTO Brisbane shop using a lathe and a dial-indicator. Figure 17 shows the step heights measured with this procedure. The payload was disassembled after this measurement and then reassembled at the range prior to launch. The necessary clearances between parts invariably lead to variations in joint quality each time a joint is assembled. To try to document this at the range following final assembly, a laser-scan of the flight vehicle was attempted just prior to launch. This was foiled by specular reflection from the polished surface of the payload. An attempt was made to scale step heights from the macrophotos shown in Figure 16. This rough analysis indicated step heights of 0.2 mm or less, consistent with the bench measurements shown in Figure 17.
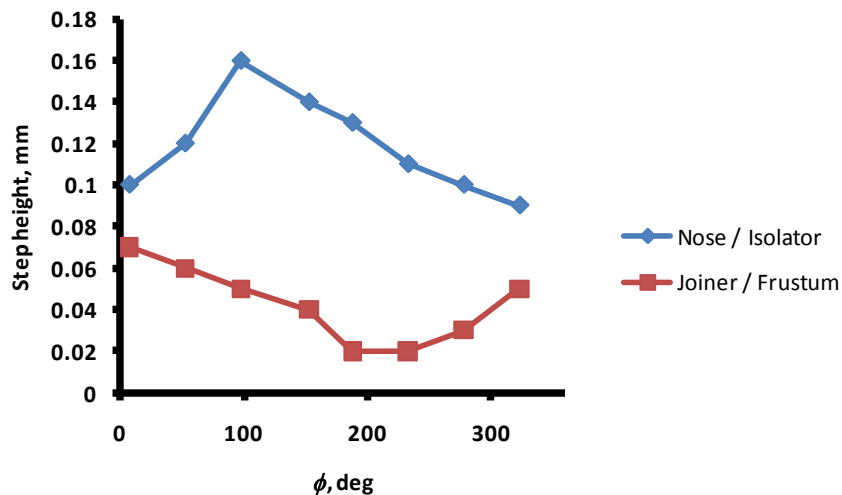
Figure 17 Circumferential variation in step heights on nose assembly

Approved for public release; distribution unlimited

Thermocouples at other circumferential stations indicate that the transition from tripped flow did not occur simultaneously around the model. A likely cause for this variation was the circumferential variation in the step heights in the nose assembly noted above. Figure 18 illustrates this variation in transition time. This figure shows measured heat transfer on the $\phi=0$ and $\phi=180$ deg rays of the cone at $x=0.3$ m. The $\phi=180$ ray is on the rough side of the cone, but the $x=0.3$ m station illustrated in Figure 18 is well upstream of the roughness element and uninfluenced by it. Flow over the $\phi=0$ deg ray dropped laminar at about 14 seconds, and flow over the $\phi=180$ ray dropped laminar at about 11.5 seconds. The large heat transfer fluctuations observed on the rough-side transducers at about $t=20$ seconds are artifacts due to poor signal-to-noise ratio.
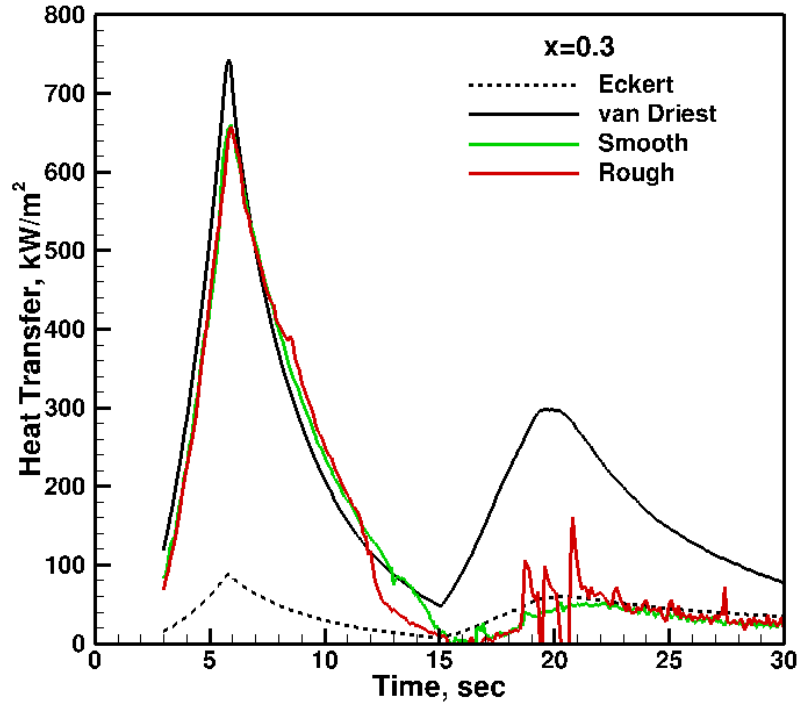

Figure 18 Rough side ($\phi=180$) and smooth-side ($\phi=0$) transitions from tripped to laminar flow

Finite-element conduction analysis further supports the supposition of tripped flow near the nosetip. In this analysis, two assumptions were made to bound the thermal state of the nosetip assembly. In the first case (hot tip), flow was assumed to trip at the nosetip / isolator junction, and transition to laminar at t=14 seconds. In the second case (cold tip), flow was assumed to trip at the joiner / frustum joint, and transition to laminar at 11.5 seconds. Laminar and turbulent heat transfer coefficients based on Eckert and van Driest heating estimates for these conditions were input into a finite-element conduction model of the nosetip. These transitions were modeled as step changes in space and time. Temperatures at two internal thermocouple locations (TLBW1 and TLBW2) were extracted from the solutions and compared to temperatures measured at these locations. TLBW1 was located in the TZM nosetip and TLBW2 was located in the joiner component. Figure 19 shows that these limiting cases bound the temperature measured on TLBW1, and the cold-tip model provides the better approximation to the TLBW2 measured temperature. Given the demonstrated circumferential non-uniformity of the heat transfer and uncertainties over trip locations, thermal contact resistances and so on, a unique solution to the measured nosetip temperatures would not be expected. However, the Figure 19 results are consistent with an early trip at some point on the nosetip. The impact of the nose joint steps is expected to diminish with time for several reasons. The boundary layer should become less sensitive to roughness as Mach number increases. The roughness Reynolds number will decrease as freestream Reynolds number drops and the boundary layer thickens. Finally, as the nose temperature increases, the step heights will decrease via thermal expansion as they were designed to do.
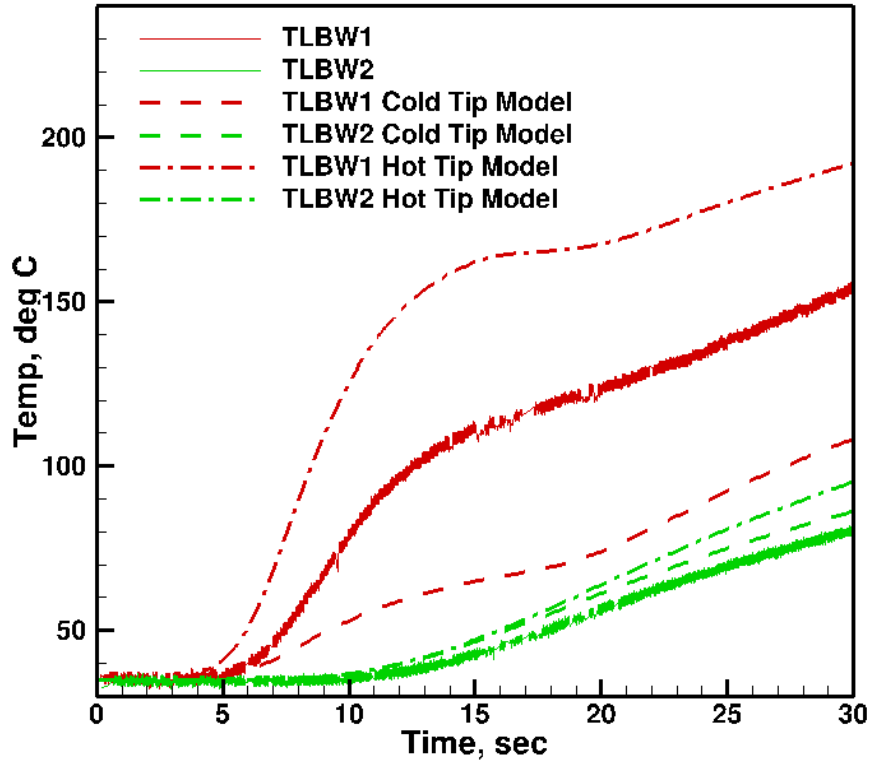
Figure 19 Measured nosetip thermocouple temperatures compared to conduction solutions for hot and cold nosetips

The suspected early trip near the nose is significant even for later times when the transition is presumed to be smooth-body. This is because the vehicle possessed no surface instrumentation upstream of x=0.3 m, so the wall temperature distribution used as a boundary condition for CFD must be inferred from heat transfer calculations. Figure 20 presents an example of the effect of tripped nosetip flow on the temperature distribution. In this example, the TOPAZ code was run using convective boundary conditions based on the BET. Several cases were examined, including fully laminar, fully turbulent and two nosetip assumptions – the "hot tip" and "cold tip" cases described above. The hot and cold tip cases were assumed to be tripped at the times and locations noted above. After this, transition was assumed to occur at an edge Reynolds number Re_e=1.8e7. This transition criterion was imposed merely to provide a rough approximation of the actual boundary conditions. The actual transition Reynolds number varied during flight. The aeroshell back face boundary condition for all cases was adiabatic. The surface temperature distribution for these cases at t=22 seconds is compared to the measured surface temperature distribution at the same time in flight for the ϕ=0-deg ray in Figure 20. In all cases the computed distributions show a temperature spike near x=0.2 m due to the low-conductivity stainless steel joiner at this location. The first five temperature measurements agree somewhat better with the hot tip model than the cold tip. This is to be expected, since transition occurred later on this ray. Somewhat more variation is observed downstream, but this is probably due to the oversimplification of the imposed transition criterion. What is most notable is the variation of 60K or more between the hot tip and cold tip cases upstream of the joiner at x=0.2m. The actual temperature distribution is ultimately unknowable, but these two cases bound the wall temperature distribution.
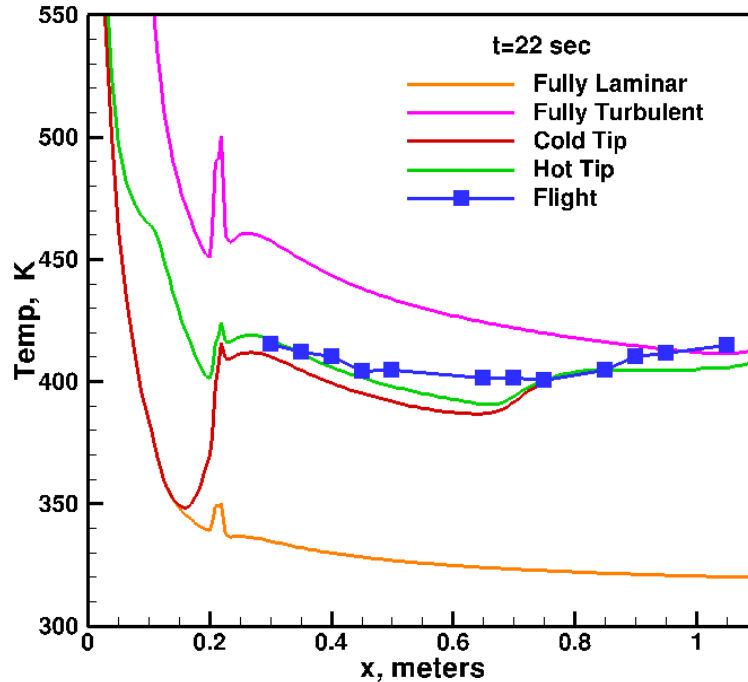
Figure 20 Calculated temperature distributions for fully laminar, fully turbulent, hot and cold tip assumptions, compared to flight measurements at t=22 seconds, ϕ=0 ray.

After transition moved off the nosetip, it progressed over the cone in a more gradual fashion. Figure 21 illustrates this progression. Thermocouples at *x*=0.9, 0.95 and 1.05 m drop from turbulent to laminar flow for 20 < *t* <23 seconds. Thermocouples between *x*=0.65 and *x*=0.85 m showed a peculiar unsteady progression between *t*=16 and 20 seconds, with multiple excursions nearly equal to the difference between laminar and turbulent heat transfer. The source of these fluctuations is unknown. Their time scale appears larger than the rotation period of the missile, and thus cannot be ascribed to variations between windward and leeward transition. In any case, the angle of attack during this period was less than 0.5-degrees. This period occurs when the second-stage booster is at maximum thrust, and might be related to disturbances arising from the motor firing, although no large oscillations were evident in the vehicle accelerometers.
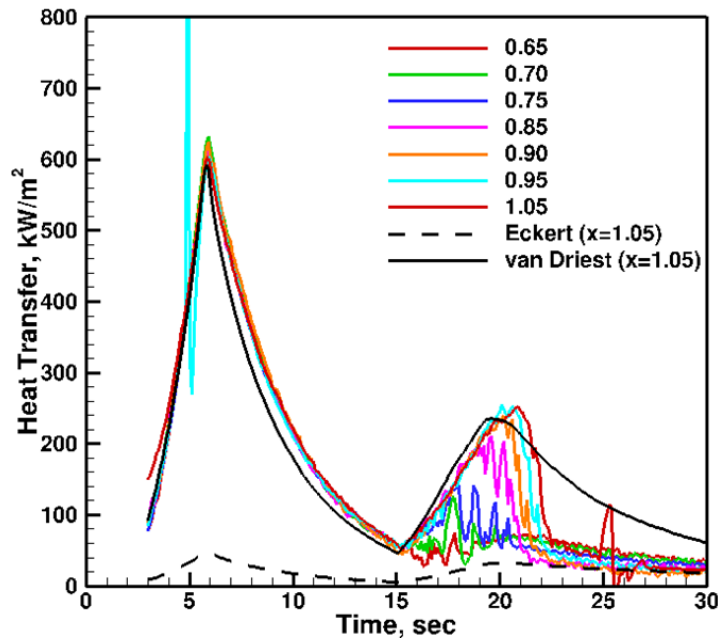
Figure 21 Smooth-side cone transition after t=15 seconds

17

The transition progression may also be visualized by examining heat transfer distributions over the cone at fixed points in time. This data presentation is an aid to visualization, since it resembles the traditional presentation of wind tunnel data. Obtaining quantitative heat transfer on the cone was not a primary objective of the HIFiRE-1 mission, but an effort was made to extract this data in order to better understand the transition process. Although the measured heat transfer data show significant scatter, up to 70% of expected laminar heat transfer, transition trends may still be extracted. Figure 22 presents heat transfer coefficient as a function of Reynolds number for times between t=19 and 22 seconds. Heat transfer coefficient and Reynolds are both referenced to freestream values. Over this period, transition moves steadily back over the cone. The maximum transition Reynolds number derived from Figure 22 occurs at 19 seconds, and is approximately 14.5×10^6 (freestream conditions) or 18×10^6 (edge conditions). Table 3 summarizes the transition times derived from smooth-side thermocouples during ascent. The near-simultaneous transition at stations at x=0.5 m and upstream is a further indication of tripped behavior. Transition upstream of x=0.85 m is difficult to define due to the oscillatory nature of the heat transfer.

Figure 22 Heat transfer distributions. Symbols – flight data, dashed – Eckert, solid – van Driest.

Table 3 Smooth Side Transition Times During Ascent

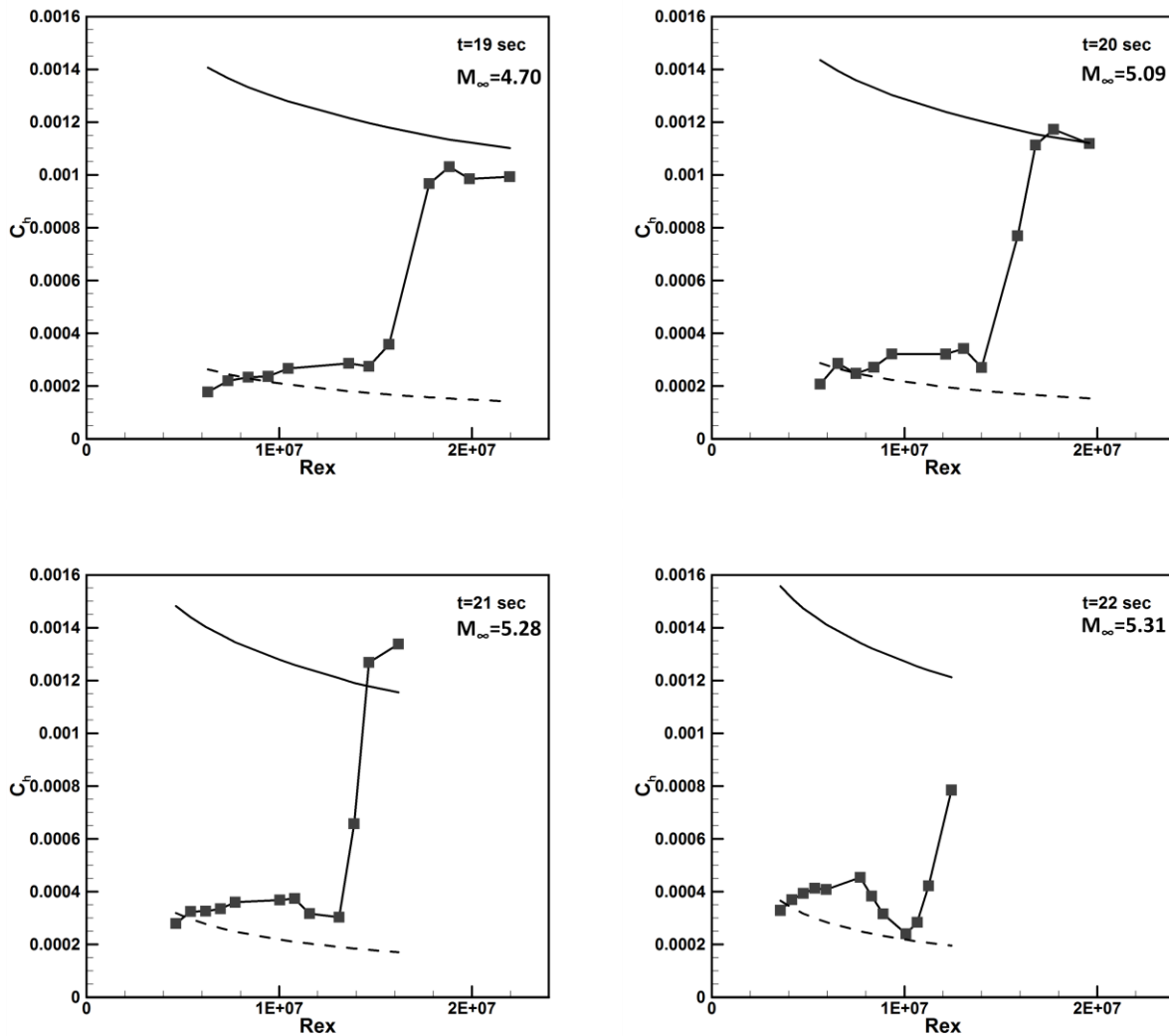| ONSET								
Axial distance from stagnation point, x	Surface arc length from stagnation point, s	Time after liftoff, t	Freestream unit Reynolds number, Re	Edge unit Reynolds, Re_e	Freestream Mach, M	Edge Mach, M_e	Re*x	Re_e*s
meters	meters	seconds	m**-1	m**-1				
0.3013	0.3037	15.59	19280000	21090000	2.75	2.6	5809064	6404244
0.3513	0.3540	15.72	19450000	21340000	2.8	2.64	6832785	7555172
0.4013	0.4044	15.5	19170000	20920000	2.72	2.56	7692921	8460331
0.4513	0.4548	15.5	19170000	20920000	2.72	2.56	8651421	9514186
0.5013	0.5052	15.71	19440000	21320000	2.8	2.64	9745272	10770107
0.6513	0.6563	17.98	20980000	24770000	3.95	3.66	13664274	16256325
0.7013	0.7067	20.23	18160000	23060000	5.07	4.61	12735608	16295726
0.7513	0.7570	20.79	17060000	21970000	5.29	4.79	12817178	16632209
0.8513	0.8578	21.51	13700000	17600000	5.24	4.74	11662810	15097153
0.9013	0.9082	21.58	13500000	17400000	5.25	4.75	12167550	15802128
0.9513	0.9585	22.38	10900000	14000000	5.23	4.74	10369170	13419612
1.0513	1.0593	22.51	10500000	13500000	5.22	4.73	11038650	14300478
END								
0.3013	0.3037	13.8	21490000	23380000	2.65	2.51	6474937	7099631
0.3513	0.3540	14.2	20710000	22490000	2.63	2.49	7275423	7962316
0.4013	0.4044	14.49	20000000	21690000	2.62	2.47	8026000	8771729
0.4513	0.4548	14.49	20000000	21690000	2.61	2.47	9026000	9864373
0.5013	0.5052	14.5	19970000	21660000	2.61	2.47	10010961	10941862
0.6513	0.6563	15.29	18920000	20540000	2.64	2.49	12322596	13480215
0.7013	0.7067	15.44	19100000	20820000	2.69	2.54	13394830	14712794
0.7513	0.7570	17.99	20990000	24790000	3.96	3.67	15769787	18767067
0.8513	0.8578	18.79	20380000	24760000	4.39	4.04	17349494	21238949
0.9013	0.9082	20.16	18260000	23140000	5.03	4.58	16457738	21015013
0.9513	0.9585	20.12	18300000	23160000	5.01	4.56	17408790	22199873
1.0513	1.0593	20.91	16320000	20990000	5.27	4.77	17157216	22234595

The symmetry of the transition process may be assessed by examining the output from transducers located at the same axial location but at different azimuthal locations. Figure 23 shows these results at several axial locations. Generally, turbulent and laminar heat fluxes are the same on all the rays within experimental scatter. The ϕ=0 and 315 deg rays show similar transition behavior. At x=0.4013 m, the ϕ=270 deg ray transition is similar to the ϕ=0 ray. At this station, the ϕ=180 deg transducer (on the rough side of the cone but upstream of the roughness element) transitions from turbulent to laminar flow earlier than the other two rays, as noted above. The ϕ=270 deg transducer at x=0.7013 m shows behavior markedly different during the period between 15-20 seconds, where it transitions much later than the ϕ=0 and 315-deg rays. At x=0.9013 m transition on the ϕ=270 deg ray is similar to the 0 and 315 deg ray, although slightly lagged. Transition on the ϕ=0 and 315-deg rays are similar. In summary, transition symmetry is good downstream of x=0.85 m (or after 18.8 seconds). Upstream (or before) this, transition shows some asymmetry. For t<18.8 seconds, transition data for the 270 deg ray is especially suspect.
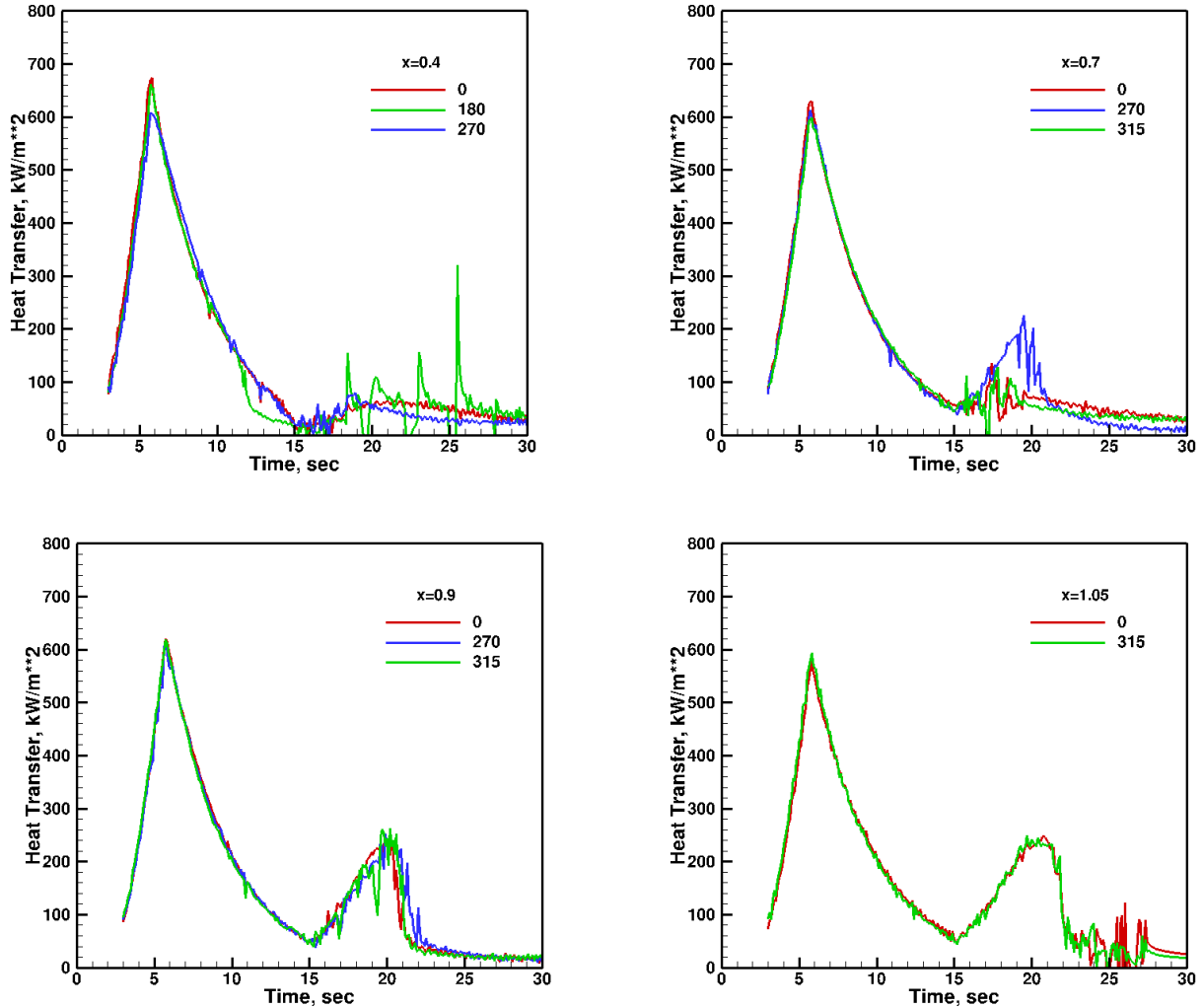
Figure 23 Axi-symmetry of heat transfer and transition

Additional insight into the transition process may be gained by examining higher bandwidth sensors. Figure 24 presents pressure fluctuations from one high-bandwidth Kulite® pressure sensor, PHBW1. Similar results were obtained from the other two smooth-side Kulites. The Kulite® pressure transducers on the cone were sampled at 60 kHz and bandpass filtered between 100 Hz and 30 kHz. Although the frequency response of the transducer was an order of magnitude lower than expected second-mode instability frequencies, the instrument at least gave some measure of the transition dynamics. The left side of Figure 24 presents dimensional pressure fluctuations. The right side of the figure shows the same data normalized by the local cone pressure. Pressure fluctuations in the turbulent boundary-layer prior to about 18 seconds mirror the local mean pressure, increasing to a maximum at first stage burnout, then declining as the vehicle coasts. Large fluctuations occurred when the second stage fired at 15 seconds, but these are largely spurious and due to interference between the second-stage exhaust plume and the TM. The large fluctuations at this time consist of numerous single-point spikes. Pressure fluctuations begin to grow until about 20-21 seconds, when they suddenly collapse. Transition was measured on the thermocouples at this *x*-station between 18.8-21.5 seconds. The growth in amplitude of the normalized pressure observed after this is an artifact caused largely by errors in assessing mean pressure at high altitude.

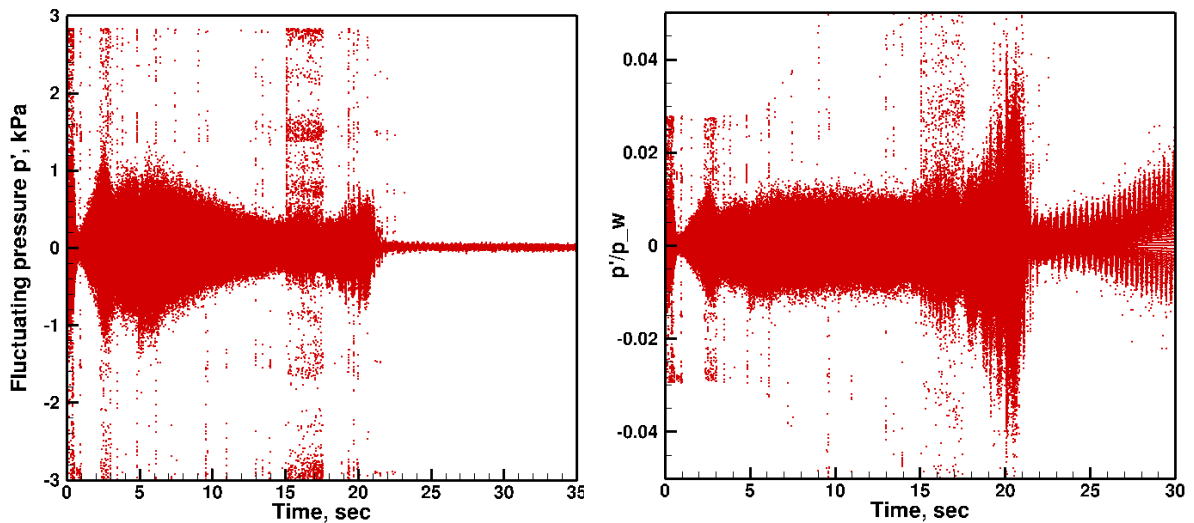**Figure 24 Fluctuating pressure PHBW1 during ascent, dimensional values (left) and normalized by local mean pressure (right).**

Figure 25 presents PHBW1 pressure fluctuations measured on the cone during ascent, expressed as an RMS value. The RMS was calculated over a moving 0.05-second window, and was normalized by the local mean pressure measured by transducer PLBW4 (green line), and also by the cone surface pressure calculated using a Taylor Maccoll solution based on the BET and BEA (blue line). Both normalizations provide consistent results until about 30 seconds, where the local mean pressure was so low that minor deviations create large variations in the normalized RMS. The boundary-layer at this location was fully turbulent (as measured by heat transfer) until approximately t=19 seconds. After this, the flow transitioned to fully laminar at t=21 seconds. The sharp rise in the RMS between 15-17 seconds is due to telemetry noise during the initial second-stage firing, and is spurious. RMS pressure fluctuations beneath the turbulent boundary layer are constant at about 0.5%. Pressure fluctuations measured beneath turbulent boundary-layers on cones range from 1-3 % in conventional wind tunnels.[26] Similar ground measurements under quiet wind conditions are not available. The rise in pressure fluctuations near 20 seconds is believed to be due to the transitional process. This local peak in pressure fluctuations near transition has also been observed in wind tunnel tests.[26]

Figure 26 shows the dynamics of the transition process during ascent as revealed by a Vatell heat transfer gauge (HT3) and a Medtherm Schmidt-Boelter gauge (HT2). Both devices are thermopiles, but the Vatell device is a thin-film gauge with a higher frequency response than the Medtherm. The manufacturer quoted time constant for the Vatell gauge is 17 microseconds. These gauges were located at ϕ=30 deg. HT3 was located at x=0.9013 m, and the HT2 was located just downstream at x=1.0013 m. These gauges reveal that the transition process that occurs between about 21.5<t<22.5 seconds is the result of multiple rapid transitions between turbulent and laminar flow. The period of laminar flow between turbulent episodes gradually increases, until the flow is fully laminar. HT2 and HT3 are well-correlated, with HT2 showing a damped response due to its lower frequency response. This degree of correlation indicates that the phenomenon is due to the flowfield, and not a characteristic of the individual transducer. The thermocouples located at x=0.9013 m indicate transition onset and end for 20.16 < t < 21.58 seconds.
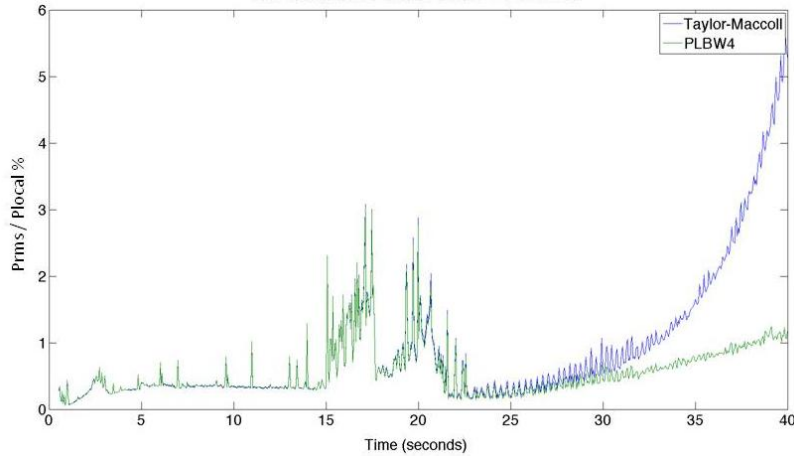
Figure 25 PHBW1 RMS pressure fluctuations
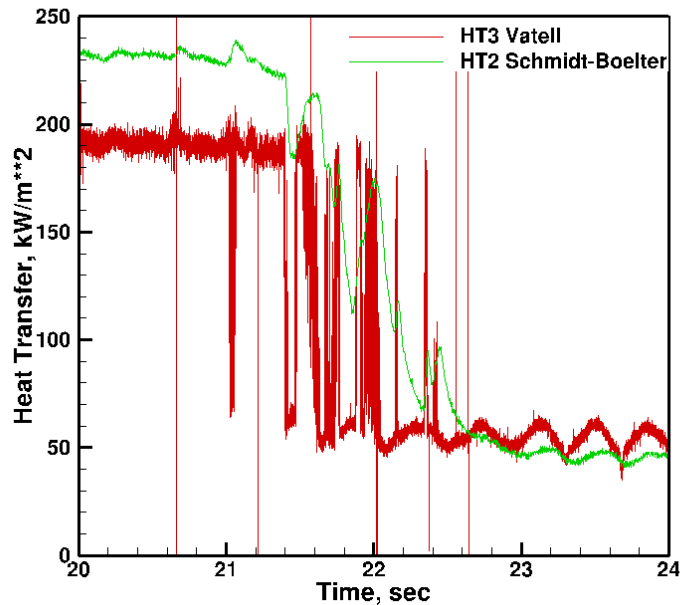
Figure 26 Comparison of Vatell heat transfer gauge and Medtherm Schmidt-Boelter heat transfer gauge.

To determine if the intermittency observed in the HT3 signal was related to the vehicle attitude, the output from this sensor was plotted as a function of roll angle for several roll periods during transition. Roll angle was derived from the pressure measurements as described above. These results are presented in Figure 27. In these plots the transducer is on the windward side at Φ_{HT3}=0, and on the leeward side at Φ_{HT3}=180 deg. Transition begins with an intermittent drop in heat transfer between 300 and 360 deg. This laminar region grows in size, and other periods of laminar flow appear as the Reynolds number drops. By the period beginning at 22.286 seconds, only one turbulent spike remains near 50-deg, and another small disturbance occurs near 100 deg. The flow appears fully laminar in the period after this. The periods of laminar and turbulent flow appear to occur at repeatable locations from roll cycle to roll cycle. Some asymmetry is evident. Some asymmetry is due to the drop in Reynolds number that occurs between the beginning and end of a roll period. For the period beginning at 21.461 seconds, edge Reynolds drops approximately 3%. Other asymmetry, such as the initial laminar period that occurs between Φ_{HT3}=300 and 360 deg cannot be explained by a Reynolds drop, and may be due to variations in the missile attitude during this time. During this period, the missile motion was not a simple spin and cone. Additional low amplitude harmonics were evident in the pressure signal. The first laminar period near Φ_{HT3}=300 deg occurs at a length Reynolds number (based on x and edge conditions) of 20.2×10^6. The last turbulent patch near Φ_{HT3}=300 deg occurs at Re=13×10^6.

22
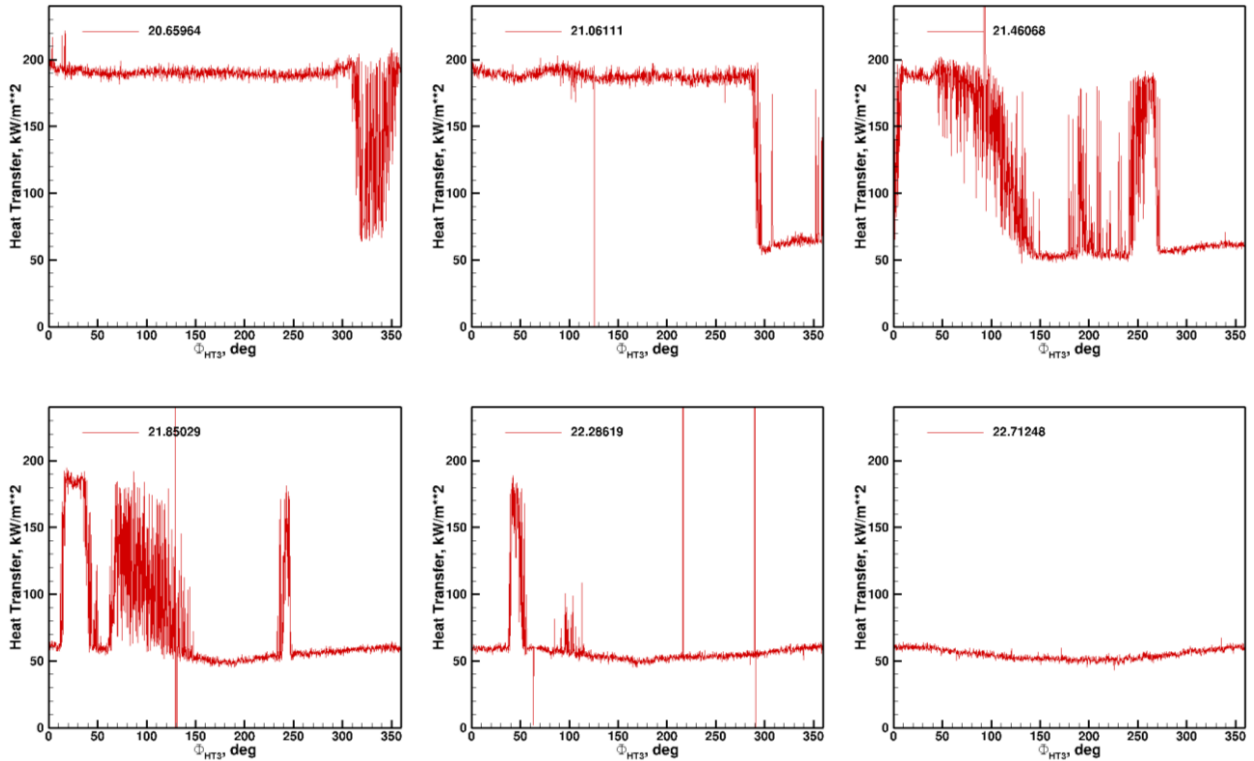
Figure 27 Detail of Vatell (HT3) output during ascent transition. Plot legend refers to approximate beginning of roll period.

The cone ray diametrically opposed to the smooth-side thermocouple ray contained a diamond-shaped trip centered at x=0.5263 m. Figure 28 shows the trip construction and a photo of the installed trip. Medtherm coaxial thermocouples are visible upstream and downstream of the trip. The planform of the trip was a square, 10 mm on each side, with radiused corners. The nominal trip height above the cone surface was 2 mm, and it was constructed of copper. The top surface was radiused to the cone centerline at x=0.5263 m so that the height of the trip did not depart substantially from 2 mm at any point.
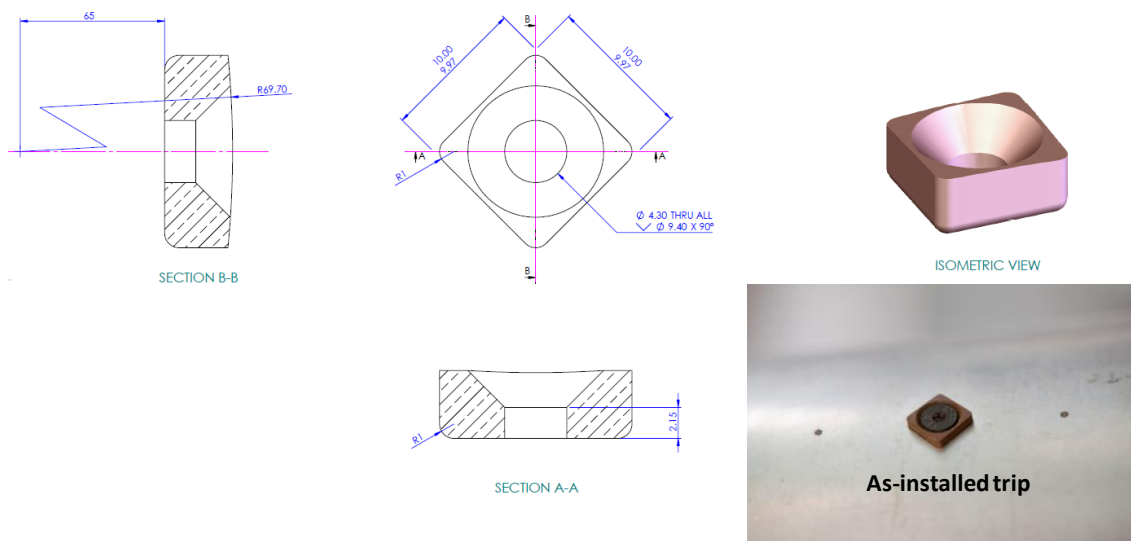
Figure 28 Boundary-layer trip. Dimensions in mm.

Most of the rough side SBLI instrumentation was on TM stream 1, and this stream experienced high noise levels during launch. Despite the high noise levels, trip effects may be extracted from these data. Figure 29 demonstrates the difference between rough-side and smooth-side transition. This figure shows data from Medtherm heat transfer gauges HT1 and HT2 on the smooth side, and HT6 and HT7 on the rough side. HT1 and HT6 were located at x=0.9013 m and displaced 15-deg from the primary thermocouple rays on their respective sides. HT2 and HT7 were located at x=1.0013 m and displaced 30-deg. Figure 29 illustrates the drop to laminar heat transfer that occurred on the smooth side between 22-23 seconds for HT1 and HT2. A number of data points from the rough-side transducers are shifted, but the overall trend is clear. Note that HT2 drops laminar about a second after HT1 since it is farther downstream. HT6 and HT7 did not attain laminar heat transfer until t=30 seconds. The difference in transition time between these thermocouples is not discernible, which is a reflection of the rapid transition movement typical of tripped transition. The trip was sized[9] to be effective at a Reynolds number Re_x=8x10^5 during descent at approximately 33 km at M=7.2. The tripped side appeared to drop laminar during ascent at h=31.5 km at M=5.68, with Re_x=9x10^5. Given the differences in Mach number and wall temperature ratio between the descent design point and the ascent effectiveness point, the agreement in Reynolds number at the trip may be coincidental. A closer examination of the trip roughness Reynolds number is called for, as well as examination of other transducers on the tripped side.
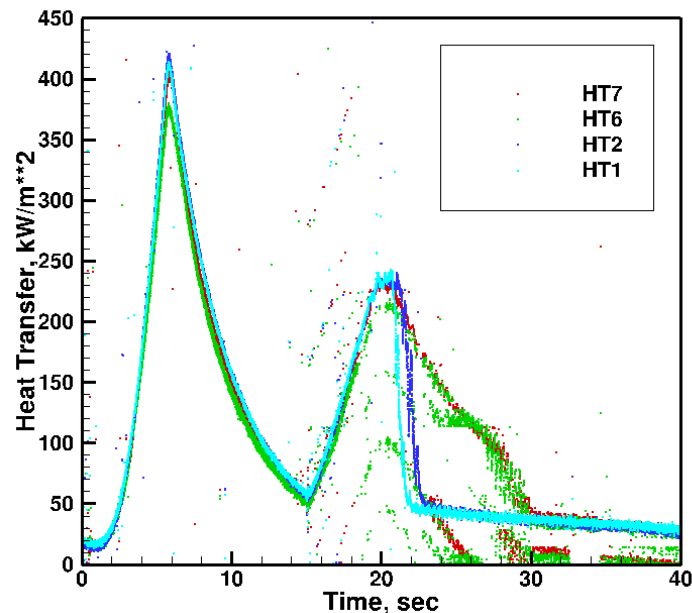
Figure 29 Comparison of rough-side (HT6, HT7) heat transfer data to smooth-side (HT1, HT2) heat transfer.

The interpretation of descent transition data is complicated by the large and time-varying AoA during this period and the thermocouple drift that preceded it. An attempt was made to extract heat transfer from thermocouples that drifted prior to entry, since the heat transfer depends on the time derivative of the temperature, not its absolute value. Figure 30 illustrates heat transfer measured with Medtherm thermocouples during descent. Heat transfer was extracted using only the front-face temperature and the adiabatic backface assumption, as described above. The measured heat transfer was compared to expected laminar and turbulent heat transfer for a cone at zero AoA at the BET conditions. The large oscillations in measured heat transfer are due to the vehicle spin at AoA, as the sensor was carried periodically between windward to leeward. Results for the transducer at x=0.5013 m are suspect, since they show much larger oscillations than the other transducers. Generally, the measured heat transfer agrees qualitatively with the predicted laminar heat transfer until it begins to rise. This point is taken as transition. Heat transfer at x=0.8013 and 0.9013 m shows large excursions after transition begins, due to transducer saturation. Transition onset is observable on these transducers, however. The drop in heat transfer after t=486 seconds on some transducers is apparently spurious. The transducer at x=0.5013 m may show a transition event after 486 seconds, but this is debatable, given the weakness of the heat transfer rise and the suspect nature of this transducer. Transducers at x=0.4013 and x=0.3013 m (not shown) do not display evidence of transition. It appears in most cases that the heat transfer minima begin to rise first, indicating a leeside-first transition. Transition onset times are summarized in Table 4. Transition times are somewhat subjective since they depend on picking a time when the

overall trend in the oscillating heat transfer begins to rise. However, they do show a trend of the transition front moving from the back to the front of the vehicle.

Figure 30 Reentry transition measured with Medtherm thermocouples.

Approved for public release; distribution unlimited

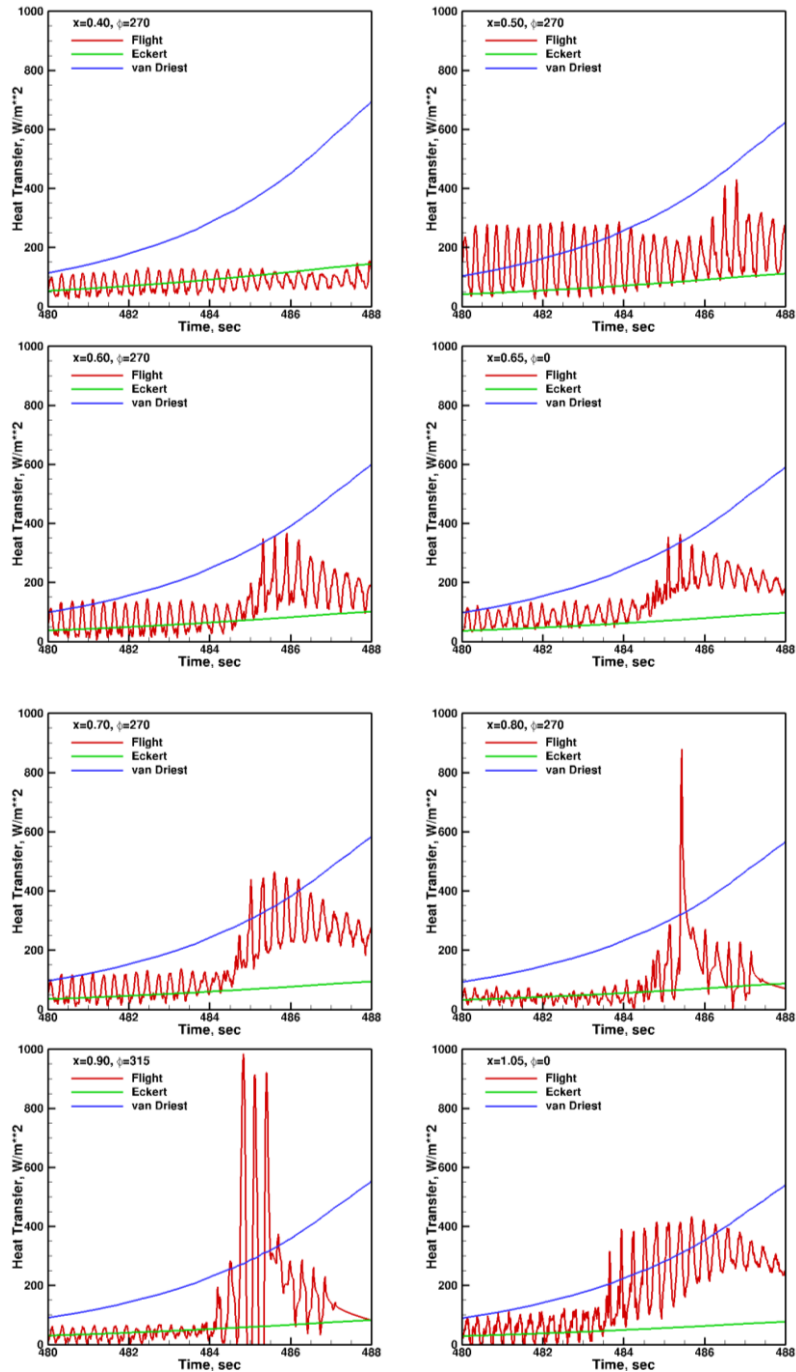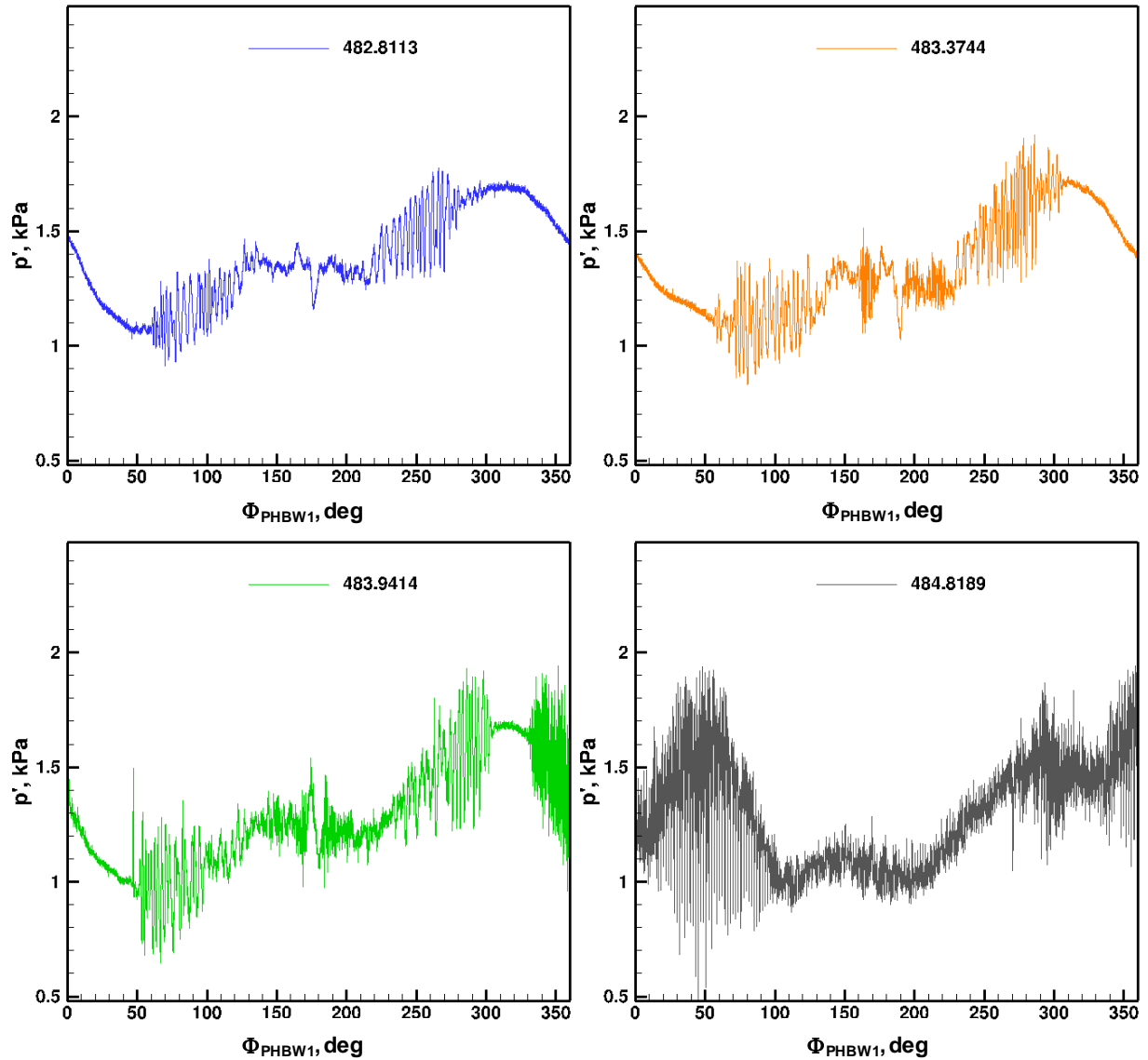## Table 4 Entry transition times measured with Medtherm thermocouples

ONSET									
ϕ	Axial distance from stagnation point, x	Surface arc length from stagnation point, s	Time after liftoff, t	Freestream unit Reynolds number, Re	Edge unit Reynolds, Re_e	Freestream Mach, M	Edge Mach, M_e	$Re*x$	Re_e*s
degrees	meters	meters	seconds	m**-1	m**-1				
270	0.4013	0.4044	488.64*	26640000	38060000	6.93	6.06	10690632	15391979
270	0.5013	0.5052	486.2**	11940000	17250000	7.07	6.17	5985522	8714087
270	0.6013	0.6059	484.56	6720000	9690000	7.01	6.13	4040736	5871320
0	0.6513	0.6563	484.38	6360000	9180000	7.01	6.12	4142268	6024750
0	0.7013	0.7067	484.54	6680000	9630000	7.01	6.12	4684684	6805197
270	0.7013	0.7067	484.55	6700000	9660000	7.01	6.12	4698710	6826397
270	0.8013	0.8074	484.50	6600000	9520000	7.01	6.12	5288580	7686613
315	0.9013	0.9082	484.20	6000000	8660000	7.00	6.12	5407800	7864737
0	1.0513	1.0593	483.48	4690000	6750000	6.97	6.10	4930597	7150239
			*Did not transition - latest measured time.						
			**Questionable						

Since the cone is at over 10 degrees AoA during the transition process, the flow should be separated and the transition front should be three-dimensional. Some of the detailed information on the shape of the transition front was filtered out of the thermocouple data, due to the limited frequency response of these instruments. The higher bandwidth instrumentation, such as the Kulite® pressure transducers and Vatell heat transfer gauges were able to resolve details of the transition front. The time records of these instruments were mapped to a roll angle around the missile (relative to the wind vector) as described above. Figure 31 presents a montage of measurements from the PHBW1 pressure transducer. Results for the other two smooth-side Kulites are very similar. PHBW1 was located at $x=$ 0.8513 m and $\phi=$10 deg. PHBW1 was referenced to the internal cone cavity and high-pass filtered from 100 Hz to 30 kHz. The times in each graph indicate the beginning of the record illustrated in the graph. At the 0 and 360 deg locations the transducer was windward, and at $\Phi_{PHBW1}=$180 deg it was on the leeward ray. A low-frequency modulation with a period equal to the roll period is apparent. Since the transducer was high-pass filtered such a low-frequency component should not be evident. It is probably present because of a combination of two factors. First, the low-pass filter possessed a finite rolloff and probably permitted some energy to pass at low frequency. Second, the low-frequency component is quite large due to the high AoA. This low-frequency component appears to be phase-shifted. The high pressure portions of the signal do not occur at $\Phi_{PHBW1}=$0 and 360 deg when the transducer is windward. This phase-shifting may have been produced by the filter or unsteady venting of the vehicle internal cavity during the roll cycle, or some combination. In summary, the low-frequency component is an artifact and should be ignored.

The higher-frequency fluctuations are more interesting. In the period beginning at $t=$482.8 seconds, two bands of fluctuations appeared between about 50-130 deg and 210-280 deg. The relatively quiescent region between about 130-210 degrees was probably in the separated region. In the period beginning at $t=$483.37 seconds, the two fluctuating bands had a greater azimuthal extent and somewhat greater amplitude. High-frequency fluctuations now began to appear between them. This trend continued in the period beginning at $t=$483.94 seconds. Also, by the end of this period, a burst of noise occurred on the windward side, probably due to transition. By $t=$484.8 seconds the signal appears fully turbulent.

Figure 31 Kulite® PHBW1 pressure measurements during descent transition

The Vatell heat transfer gauge HT3 showed similar behavior. The output from this gauge is illustrated in Figure 32. This transducer was located at x=0.9013 m and ϕ=30 deg. For comparison, each graph in Figure 32 contains limiting cases t=469.84 seconds and t=485.11 seconds, corresponding to an early time where the signal is essentially electronic noise and a later time when the signal is fully turbulent. The two earliest periods shown in Figure 32 display a disturbed heat transfer near Φ_{HT3}=180 deg, presumably due to separation, with heat transfer fluctuations on either side at about the same locations where fluctuations occurred in PHBW1. These fluctuations grew with time. Windside transition occurred at the end of the t=483.65 period, slightly before it appeared on PHBW1. Presumably, this is due to the more downstream location of HT3. By 484.82 seconds, flow over HT3 was mostly turbulent, except for small patches of transitional flow between 50-60 deg and 270-300 deg.
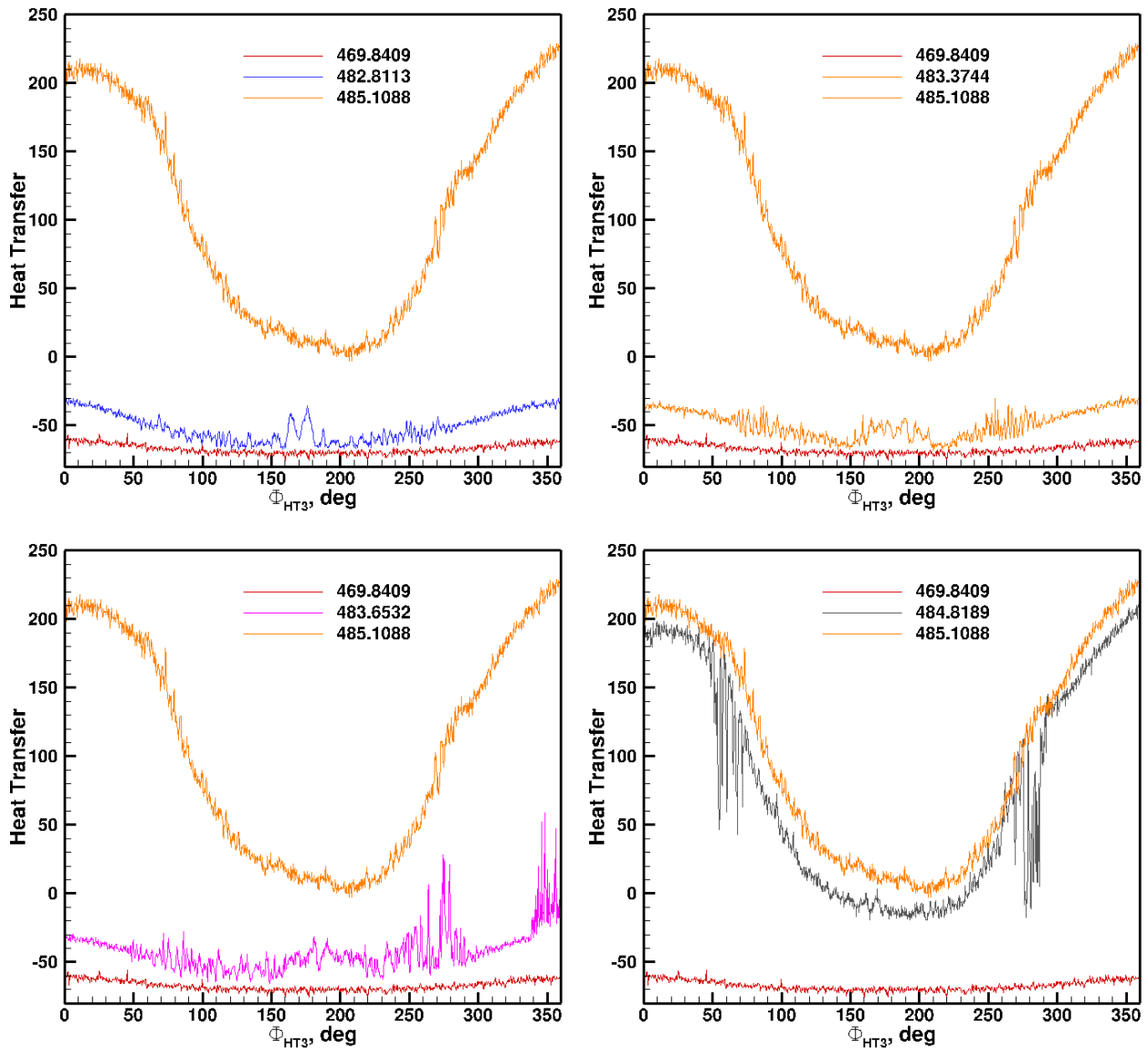
Figure 32 Vatell heat transfer guage HT3 signal during descent.

Closer inspection of both the PHBW1 and HT3 outputs show that the fluctuations preceding fully turbulent flow were periodic. Figure 33 demonstrates the periodicity apparent in both signals. The PHBW1 fluctuations were more regular than those measured on the HT3. When examined in the time domain, the fluctuations appear to be relatively low-frequency. PHBW1 fluctuations were on the order of 300 Hz, two orders of magnitude lower than the second-mode frequency. This raises the question of whether the periodic disturbances in the transducer signals were created as the transducers rotated beneath stationary crossflow waves, or whether they are due to some other phenomenon. In the angular coordinates of Figure 33, these disturbances have a period of 3-5 degrees. At this station, this angular dimension would translate to a wavelength of about 5-9 mm. Further analysis, including 3D stability calculations to compare wavelengths, is necessary to answer this question.
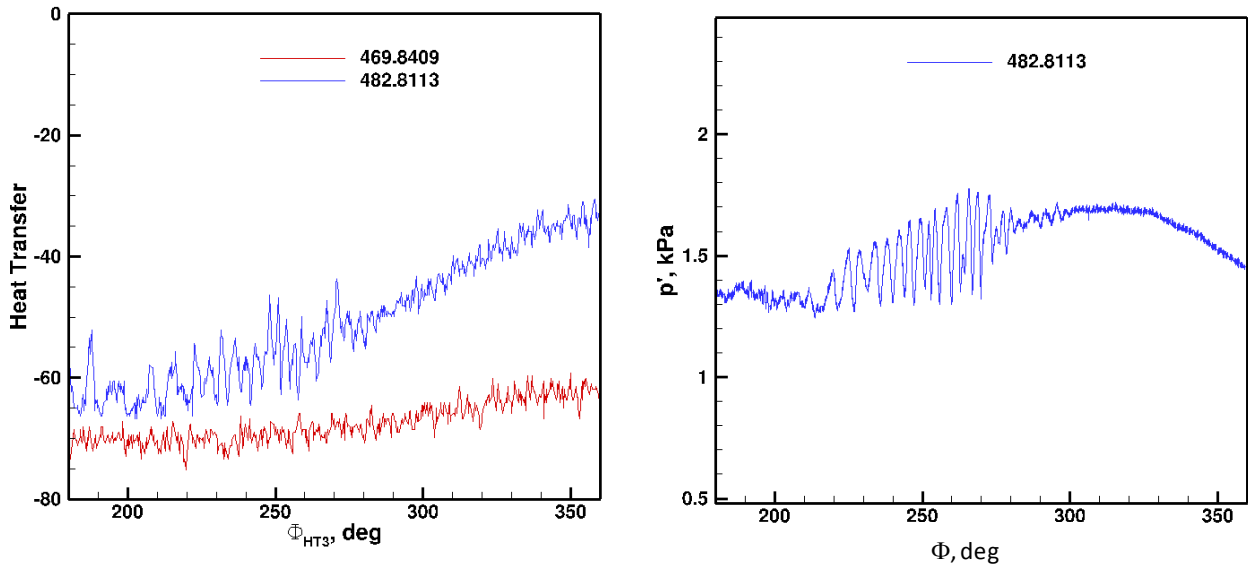
Figure 33 Detail of heat transfer and pressure fluctuations during t=482.81 roll cycle

The angular location of disturbed regions as described above may be combined with the freestream Reynolds number to create a map of the disturbance front. This map, shown in Figure 34, demonstrates that the PHBW1 detects disturbances earlier than the HT3. However, once disturbances began to register on the HT3, their location agreed fairly well with that measured with PHBW1. Two lobes of disturbances appear near 90-deg and 250-deg on PHBW1 as early as $Rex=2x10^6$. The angular extent of these regions increases as the Reynolds number increases, until they merge on the centerline. This merger is not well-defined in time, but seems to occur near $Rex = 4x10^6$. Windward transition appears just under $Rex=5x10^6$. The windward transition front merges with the side lobes near $Rex=6.5x10^6$. Transition fronts with a similar topology of lobes and indentations have been observed in wind tunnel experiments on cones at AoA, although they did not exhibit the degree of indentation observed on HIFiRE-1.[27,28]
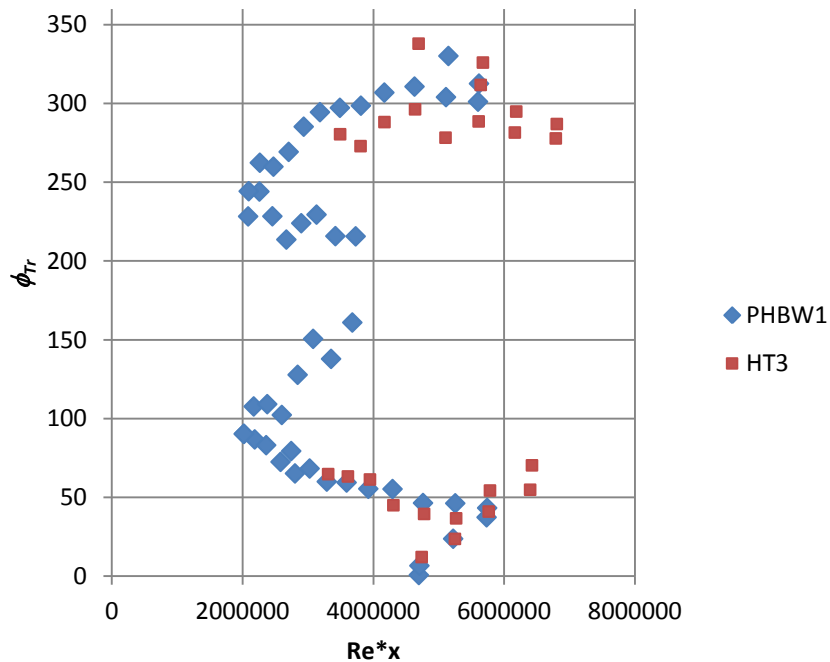

Figure 34 Map of disturbance front on vehicle during descent

VI. SBLI Results

Since the SBLI experiment was secondary to the BLT experiment, it received less attention during analysis, and the SBLI results are consequently less mature than those for the BLT. Also, there is no readily accessible theory against which to compare SBLI results. In lieu of a computation, flight data are compared to a limited set of ground test data. Several sample points taken during ascent illustrate the nature of the results.

Low-bandwidth pressure distributions in the SBLI measured at four times during ascent are illustrated in Figure 35. Pressures were normalized by the most upstream transducer, PLBW17. During the period shown, which was during coast, Mach and freestream unit Reynolds decreased from 3.4 and 4.23×10^7 per meter, respectively, to 2.83 and 2.88×10^7 per meter. The pressure distribution is typical of a turbulent separated shock boundary-layer interaction. The upstream influence in the interaction moves forward during ascent as the Reynolds number drops. No clear pressure peak in the reattachment is observable. Wind tunnel measurements at M=7 indicated that the peak pressure occurred downstream of the reattachment location as observed in schlieren.[11] Since the HIFiRE-1 flare was sized for reentry conditions, it is not clear if reattachment occurred on the flare face at the conditions in Figure 35.
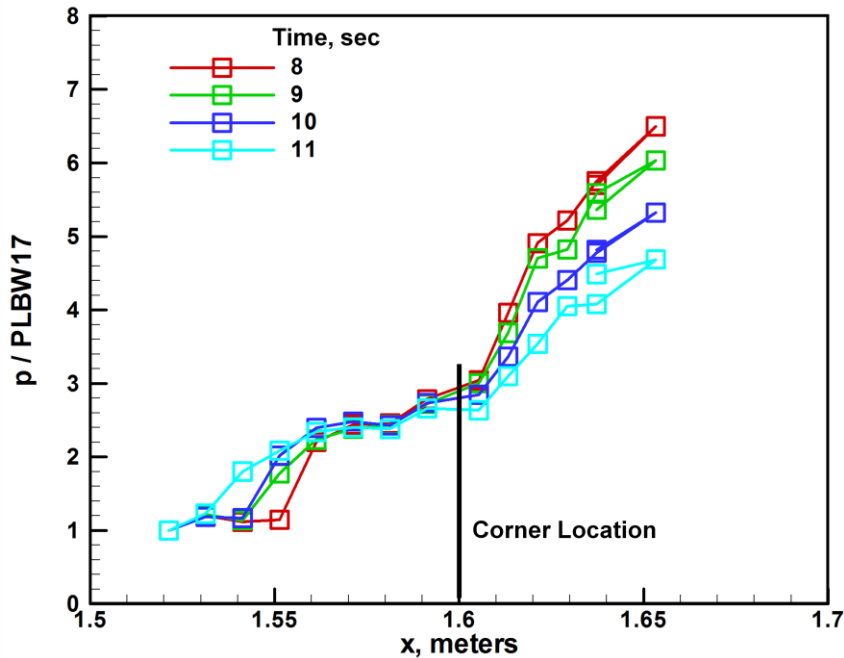

Figure 35 Low-bandwidth pressures in SBLI

Sample heating distributions for the SBLI are shown in Figure 36. The flight data were compared to ground test results from CUBRC[11] and LaRC.[13] The CUBRC model in this case deviated from the as-flown HIFiRE configuration, in that the flare was extended farther downstream to ensure that relaxation downstream of attachment was captured. This comparison was made using flight data taken at t=20 seconds. Freestream Mach number for HIFiRE at this time was 5.09. This was the highest ascent Mach number (latest ascent time) that appeared to be free from transitional effects on the untripped side of the payload. Since each data set was obtained at a different Mach and Reynolds number, the comparison among the data sets can only be qualitative. The length Reynolds number, based on freestream conditions and distance to the flare / cylinder intersection for HIFiRE, LaRC and CUBRC was 29.6×10^6, 2.2×10^6, and 15.3×10^6, respectively. The LaRC model was tripped on the forecone to produce a turbulent boundary-layer. It should be noted that the heat transfer data for flight were derived using a 1D inverse thermal analysis. Axial conduction effects have not been assessed yet, and may be significant due to the large axial temperature gradients on the flare. In general, the HIFiRE SBLI flight data are congruent with the wind tunnel data in terms of overall heat transfer and size of the interaction. Additional analysis and test should provide more quantitative comparison with wind tunnel results.

Figure 37 compares the HIFiRE-1 SBLI pressure distribution measured at 20 seconds to the CUBRC results for the same conditions shown in Figure 36. Pressure measurements were not available from the LaRC tests. The HIFiRE pressures are normalized by the most upstream measurement station in the SBLI, and the CUBRC results are normalized by a transducer in a similar location. These results are consistent with the heat transfer results shown

in Figure 36. The normalized HIFiRE pressures were slightly higher than those measured at CUBRC, and the peak pressure was not as high.
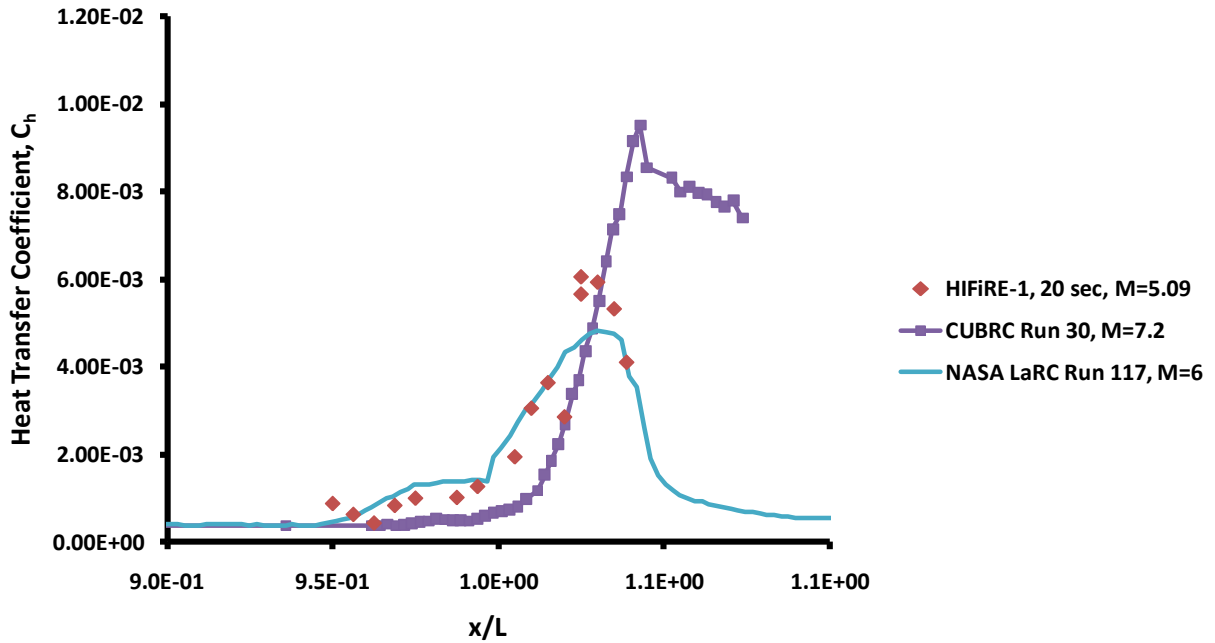

Figure 36 Heat transfer coefficient for HIFiRE-1 SBLI in flight and in wind tunnel
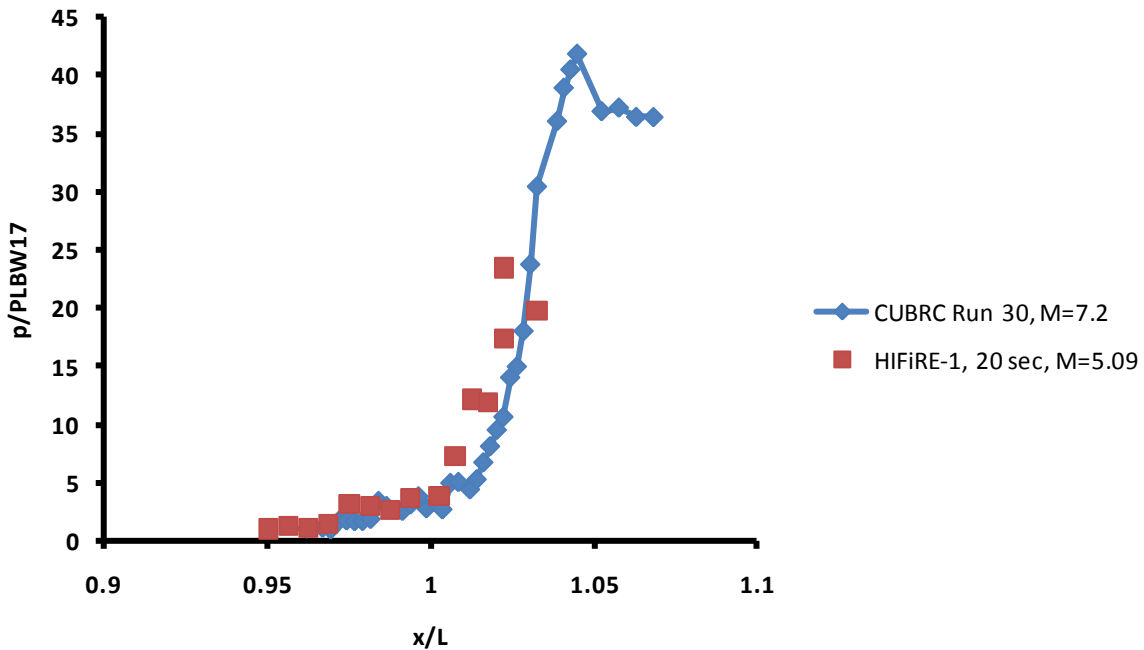

Figure 37 Normalized pressure distribution for HIFiRE-1 SBLI and CUBRC ground test

The pressure signals in the SBLI also displayed dynamic behavior over a range of time scales. Figure 38 shows the ascent time history of pressure for one transducer, PLBW20, in the SBLI. This transducer was on the cylinder 50 mm upstream of the cylinder / flare corner. After peaking at about three seconds, the overall pressure level dropped as the vehicle ascended. Pressure then rose again between about 8-10 seconds. This rise was probably due to the separation shock moving upstream over the transducer. Some unsteadiness in the pressure signal is noticeable during this period. The time scale of this unsteadiness was similar to the roll period of the vehicle, and probably

arose from a slight non-zero AoA that caused the transducer to move between the windward to leeward sides of the missile as it rolled.
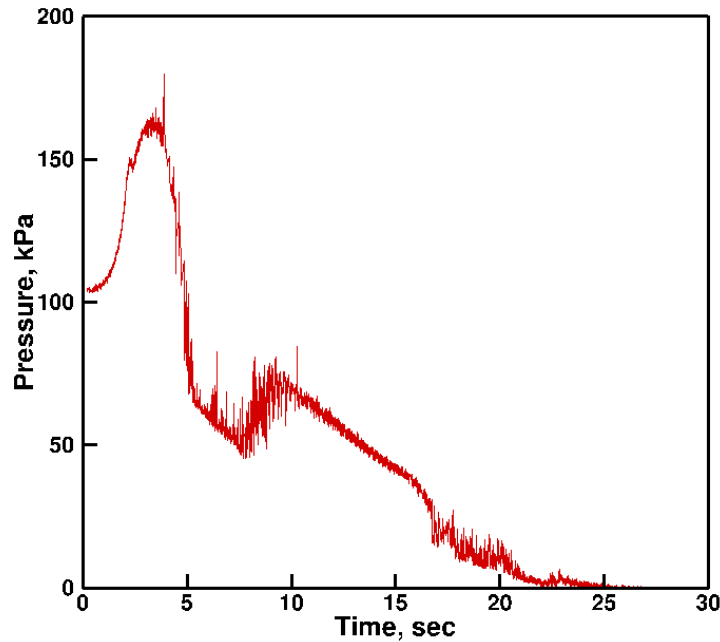

Figure 38 Low-bandwidth pressure signal in shock-boundary-layer interaction during ascent.

Unsteadiness on a shorter temporal scale was observed with high-bandwidth pressure transducers. The Kulite® pressure transducers in the SBLI all saturated at some point during ascent. The period of time spent saturated depended on the transducer location. It is unclear if this saturation was due to actual pressure fluctuations or some other phenomenon. Some amount of saturation during ascent was expected since the transducers were sized for measurements during the descent phase of the flight at lower dynamic pressure. Figure 39 shows an example for PHBW8, situated on the cylinder upstream of the flare at x=1.5413 m. The cylinder / flare corner was located at $x=$ 1.6013 m. Saturation occurred between 3-5 seconds during maximum dynamic pressure and again between 9-13 seconds. Despite periods of transducer saturation, useful periods of data remain. A major objective of the SBLI experiment was to search for low-frequency oscillations in the separation-induced shock. Shock oscillation is manifested as a bimodal pressure distribution.[29] The period between 5 and 8 seconds, shown in detail on the right of Figure 39, is demonstrably bimodal and unsaturated, and suitable for further analysis.

Figure 40 illustrates the power spectral density derived from PHBW8 at several points in time, before, during and after the period of bimodal pressure distribution noted in Figure 39. Each PSD is taken over a 0.05-second window. The PSDs before and during the bimodal episode showed a strong spectral content below 2 kHz, peaking at less than 200 Hz. This low-frequency periodicity is clearly evident in the time-series of Figure 39 between 5.2 and 5.25 seconds, and is perhaps associated with an aerodynamic or structural mode of the missile. It is far higher than the roll frequency of the missile at this time, which was approximately 6 Hz. Inspection of the time series shows that the peak in the spectrum at about 3 kHz during the period from 6.2-6.25 seconds is associated with the bimodal pressure fluctuations. CFD is necessary to calculate the incoming boundary-layer thickness and edge velocity to scale the frequency so that it may be compared to wind tunnel test results. Conditions at t=6.2 seconds are freestream M=3.43 and freestream unit Reynolds number of 5.6×10^7 per meter, or a length Reynolds number of 9×10^7 at the cylinder-flare intersection.
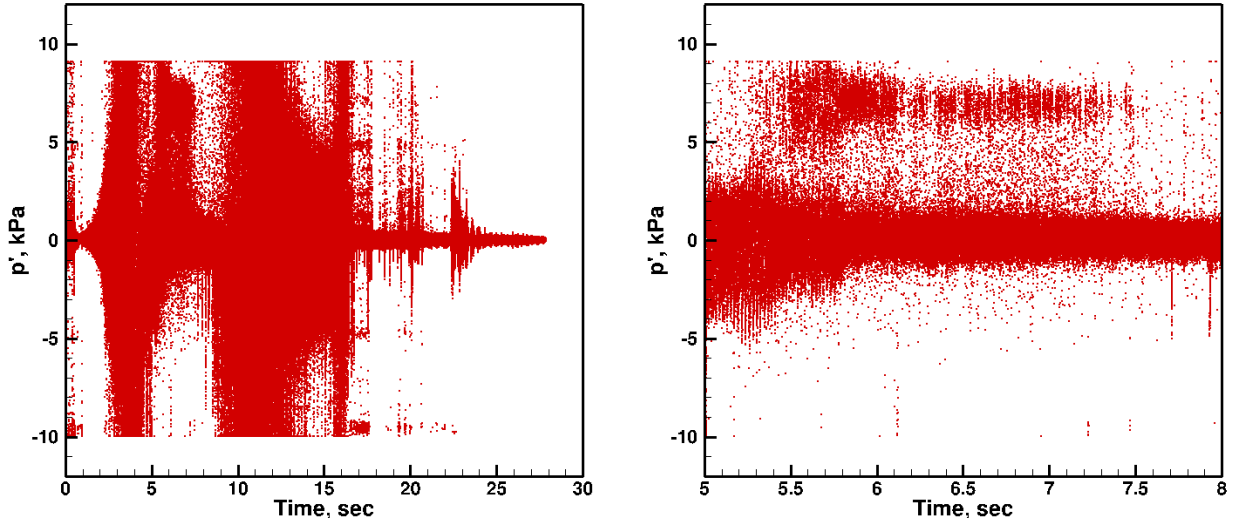
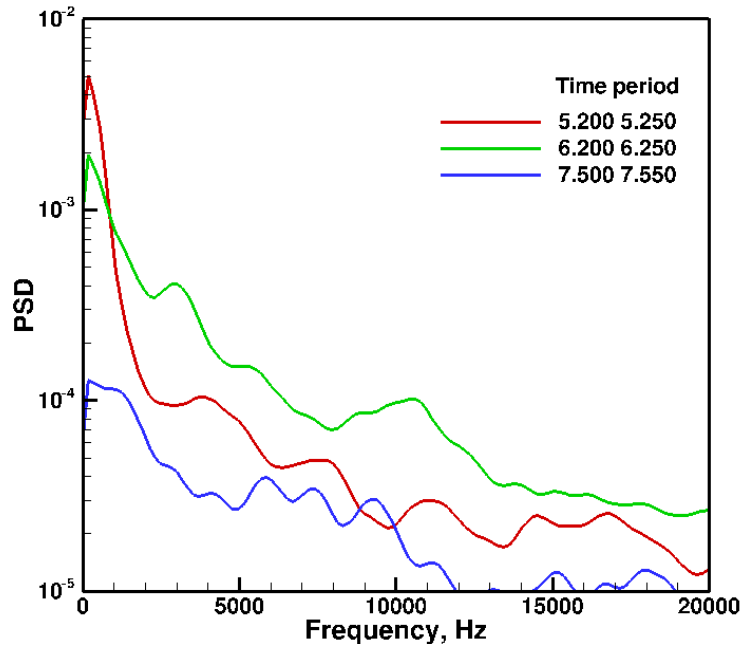**Figure 39 PHBW8 pressure fluctuations during ascent (left) and detail during period of interest (right)**

Figure 40 Power spectral densities during ascent

VII.   Conclusions and Additional Work

The HIFiRE-1 flight successfully acquired surface pressure, temperature and heat transfer data at freestream Mach numbers up to 7. The flight met its two primary objectives, to measure second-mode transition and to measure fluctuating pressures in a turbulent shock-boundary-layer interaction.

The flight suffered several system malfunctions, but each was compensated for in some way. The GPS system failed, requiring the trajectory be reconstructed using a BET process. The exoatmospheric pitch-over maneuver also failed, resulting in an AoA of over 10 deg during reentry. In this case, the ascent phase provided useful low angle of attack transition and SBLI data. High-bandwidth pressure transducers in the SBLI all saturated at some point during ascent, but intermittency in the pressure signal was observed during periods when the transducers were not saturated. A number of the primary thermocouples used to measure heat transfer and transition on the cone drifted after ascent. Despite this, enough thermocouples survived to reconstruct the transition process during reentry.

Data obtained during the later stages of ascent appear to provide clean transition measurements useable for calibrating the *N*-factor transition correlations. Stability calculations[15] indicated N-factors of about 14, indicative of second-mode transition. The transition process during ascent showed some intermittency, perhaps due to subtle variations in the vehicle flight conditions. The high bandwidth pressure and heat transfer transducers possessed frequency response adequate to define transits between laminar and turbulent regions during entry. These measurements were used to construct a map of the transition front in terms of roll angle and Reynolds number. Fluctuations with a well-defined periodicity were measured during entry, perhaps as a result of transducers transiting stationary disturbances as the vehicle spun.

HIFiRE-1 demonstrated new instrumentation for transition measurement. Medtherm coaxial thermocouples with hand-formed "sliver junctions" survived and performed well. Kulite® pressure transducers and Vatell heat transfer gauges were able to resolve dynamic processes during transition. Medtherm Schmidt-Boelter gauges also provided heat transfer data with a response intermediate between coaxial thermocouples and the Vatell gauges.

The HIFiRE-1 flight produced a large amount of data. The analysis reported in this paper has assessed the data quality and provided some initial results. A number of analyses might now be conducted to better understand the phenomena observed on this flight:

High-bandwidth transducers. The high bandwidth transducers can yield a large amount of additional data. Those on the cone may provide some indication of intermittency in the transition process. Those in the SBLI will be assessed for quality and be subjected to spectral analysis and probability density analysis to discern shock fluctuations. Transducers may be cross-correlated to infer larger-scale motions in the SBLI.

Thermal analysis. Thermal analysis has been confined to axisymmetric analysis of the cone using heat transfer rates inferred from Eckert and van Driest theories. A full 3D analysis could be performed using the measured flight heat transfer, taking into account the mid-body boundary-layer trip. Analysis of the SBLI and flare would be especially interesting.

Heat transfer. Heat transfer has been derived from 1D and axisymmetric inverse analysis. This analysis is probably adequate for the cone, but significant axial heat transfer may have occurred in the SBLI. A 3D inverse analysis would be helpful in understanding these effects.

Boundary layer trip. The tripped side data suffered from high TM noise, but numerous transducers appear to show useful data. These data should be subject to further analysis. Computation of correlating parameters would be helpful.

High AoA transition. Since the higher bandwidth transducers appear to have resolved the transition front and perhaps instabilities, further analysis of transition under these conditions would be very interesting. Three-dimensional stability analysis would help in determining the nature of the periodic fluctuations observed prior to transition. Wind tunnel tests would also help resolve this question, and also provide the overall shape of the transition front. Additional CFD and testing might also help refine AoA estimates.

SBLI. Heat transfer and pressure distributions will be derived from the flight data at a variety of flight times. These may then be compared to wind tunnel test results and computation.

High altitude data. Some pressure and temperature sensors appeared to show roll-related modulation as high as 68 km. It remains to be seen if these fluctuations are indeed flow-related, and if the measurements are of sufficient accuracy to be useful as verification data. Also, the accuracy of AoA measurements at this altitude has not been assessed, and the balloon sounding data did not reach this altitude. The possibility of retrieving data at these high altitudes is intriguing, however, and it would be worthwhile to explore the usability of the data.

Acknowledgments

References

[1] Dolvin, D. "Hypersonic International Flight Research and Experimentation (HIFiRE) Fundamental Science and Technology Development Strategy," AIAA Paper 2008-2581, April 2008.

[2] Dolvin, D. J., "Hypersonic International Flight Research and Experimentation Technology Development and Flight Certification Strategy," AIAA paper 2009-7228, October 2009.

[3] Kimmel, R. L., Adamczak, D., Gaitonde, D., Rougeux, A., Hayes, J. R., "HIFiRE-1 Transition Experiment Design," AIAA paper 2007-0534, January 2007.

[4] Wadhams, T. P., MacLean, M. G., Holden, M.S., and Mundy, E., "Pre-Flight Ground Testing of the Full-Scale FRESH FX-1 at Fully Duplicated Flight Conditions," AIAA paper 2007-4488, June 2007.

[5] Johnson, H. B., Alba, C. R., Candler, G. V., MacLean, M., Wadhams, T, and Holden, M. "Boundary Layer Stability Analysis of the Hypersonic International Flight Research Transition Experiments," AIAA Journal of Spacecraft and Rockets, vol. 45, no. 2, March-April 2008.

[6] Holden, M. S., Wadhams, T. P., MacLean, M., "Experimental Studies in the LENS Supersonic and Hypersonic Tunnels for Hypervelocity Vehicle Performance and Code Validation," AIAA paper 2008-2505, April 2008.

[7] Kimmel, R. L., "Aerothermal Design for the HIFiRE-1 Flight Vehicle," AIAA paper 2008-4034, June 2008.

[8] Casper, K. M., Wheaton, B. M., Johnson, H. B., and Schneider, S. P., "Effect of Freestream Noise on Roughness-Induced Transition at Mach 6," AIAA paper 2008-4291 June 2008.

[9] Kimmel, R. L., "Roughness Considerations for the HIFiRE-1 Vehicle," AIAA Paper 2008-4293, June 2008.

[10] Alba, C. R., Johnson, H. B., Bartkowicz, M. D., Candler, G. V., and Berger, K. T. "Boundary-Layer Stability Calculations for the HIFiRE-1 Transition Experiment," AIAA Journal of Spacecraft and Rockets, vol. 45, no. 6, November-December 2008, pp. 1125-1133.

[11] Wadhams, T. P., Mundy, E., MacLean, M. G., and Holden, M. S., "Ground Test Studies of the HIFiRE-1 Transition Experiment Part1: Experimental Results," AIAA Journal of Spacecraft and Rockets, vol. 45, no. 6, November-December 2008, pp. 1134-1148.

[12] MacLean, M., Wadhams, T., Holden, M., and Johnson, H., "Ground Test Studies of the HIFiRE-1 Transition Experiment Part 2: Computational Analysis," AIAA Journal of Spacecraft and Rockets, vol. 45, no. 6, November-December 2008, pp. 1149-1164.

[13] Berger, K. T., Greene, F. A., Kimmel, R. L., Alba, C., and Johnson, H., "Erratum on Aerothermodynamic Testing and Boundary-Layer Trip Sizing of the HIFiRE Flight 1 Vehicle," AIAA Journal of Spacecraft and Rockets, vol. 46, no., 2, March-April, 2009, pp. 473-480.

[14] Adamczak, D., Alesi, H., Frost, M., "HIFiRE-1: Payload Design, Manufacture, Ground Test, and Lessons Learned," AIAA paper 2009-7294, October 2009.

[15] Li, F., Choudhari, M., Chang, C., Kimmel, R., Adamczak, D., "Transition Analysis for the HIFiRE-1 Flight Experiment," AIAA paper pending, June 2011.

[16] Brown, M. S., and Barhorst, T. F., "Post-Flight Analysis of the Diode-Laser-Based mass Capture Experiment ONbard HIFiRE Flight 1," AIAA paper 2011-2359, April 2011.

[17] "NASA Sounding Rocket Program Handbook," 810-HB-SRP, Sounding Rockets Program Office, Suborbital & Special Orbital Projects Directorate, Goddard Space Flight Center, Wallops Island Flight Facility, June 2005.

[18] Smart, M. K., Hass, N. E., and Paull, A., "Flight Data Analysis of the HyShot 2 Scramjet Flight Experiment," AIAA Journal, vol. 44, no. 10, October 2006, pp. 2366-2375.

[19] Walker, S., and Rodgers, F., "The Hypersonic Collaborative Australia/United States Experiment (HyCAUSE)," AIAA paper 2005-3254, May 2005.

[20] Wiesel W. E., Spaceflight Dynamics, 2nd Ed., McGraw-Hill Series in Aeronautical and Aerospace Engineering, McGraw-Hill, pp. 138-140, 1997.

[21] Adamczak, D., Kimmel, R. L., Paull, A., Alesi, H., "HIFiRE-1 Flight Trajectory Estimation and Initial Experimental Results," AIAA paper 2011-2358, May 2011

[22] Van Driest, E. R., "Turbulent Boundary Layer in Compressible Fluids," *Journal of the Aeronautical Sciences*, vol. 18, no. 3, March 1951, pp. 145-160, 216.

[23] Eckert, E. R. G., "Engineering Relations for Friction and Heat Transfer to Surfaces in High Velocity Flow," *Journal of the Aeronautical Sciences*, vol. 22, Aug., 1955, pp. 585-587.

[24] Thompson, P.A., Compressible Fluid Dynamics, McGraw-Hill Book Company, New York, New York, 1972, pp. 487-490.

[25] Smart, M. K., Hass, N. E., and Paull, A., "Flight Data Analysis of the HyShot 2 Scramjet Flight Experiment," *AIAA Journal*, vol. 44, no. 10, October 2006, pp 2366-2375.

[26] Casper, K. M., Beresh, S. J., Henfling, J. F., Spillers, R. W., Pruett, B., and Schneider, S. P., "Hypersonic Wind-Tunnel Measurements of Boundary-Layer Pressure Fluctuations," AIAA paper 2009-4054, June 2009.

[27] Holden, M., Bower, D., and Chadwick, K., "Measurements of Boundary Layer Transition on Cones at Angle of Attack for Mach Numbers from 11 to 13," AIAA-95-2294, June 1995.

[28] Swanson, E. O., and Schneider, S. P., "Boundary-Layer Transition on Cones at Angle of Attack in a Mach-6 Quiet Tunnel," AIAA paper 21010-1062, January 2010.

[29] Dolling, D. S. and Murphy, M. T., "Unsteadiness of the Separation Shock Wave Structure in a Supersonic Compression Ramp Flowfield," AIAA J., vol. 21, no. 12, pp. 1628-1634, December 1983.

Approved for public release; distribution unlimited